15

Automated Three-Dimensional Image Analysis Methods for Confocal Microscopy

Badrinath Roysam, Gang Lin, Muhammad-Amri Abdul-Karim, Omar Al-Kofahi, Khalid Al-Kofahi, William Shain, Donald H. Szarowski, and James N. Turner

INTRODUCTION

Image analysis is the process of making **quantitative** structural and functional measurements from an image. With the widespread availability of three-dimensional (3D) microscopy, coupled with a growing trend towards quantitative studies, there is an increasing need for 3D image analysis. The goal of this chapter is to describe 3D image analysis techniques, with an emphasis on highly automated methods.

Figure 15.1 shows two examples of 3D image analysis. In the first (top row), confocal microscopy is used to image cell nuclei from the rat hippocampus using a DNA stain, and the transcription products (mRNA) of an immediate early gene (*Arc*) are labeled by fluorescence *in situ* hybridization (FISH) (Guzowski *et al*., 1999; Guzowski and Worley, 2001; Vazdarjanova *et al*., 2002). The table on the right is a partial display of the results of the 3D image analysis. It consists of a table listing all the nuclei, their morphometric features, and the amount of FISH signal associated with each nucleus. The second example (lower row) illustrates 3D analysis of a dye-injected neuron imaged by confocal microscopy (So *et al*., 2000; Brown *et al*., 2001; Al-Kofahi *et al*., 2002; Jain *et al*., 2002). Various windows in this screen view are from a software system (Neuroexplorer, Microbrightfield, Inc.) that indicates automatically generated traces, branch points, and morphological measurements.

The motivation for 3D image analysis is to achieve correct morphometry of biological structures without the errors associated with projecting onto a two-dimensional (2D) plane. For example, it is difficult to distinguish overlapping objects from 2D projections, whereas 3D imaging provides richer segmentation cues. Many structures, such as neurons and vasculature, are often thicker than the depth-of-field of the microscope, necessitating 3D imaging and analysis. Often, non-planar regions are of interest. For such cases, optical sectioning via confocal microscopy better preserves 3D spatial relationships compared to physical sectioning, and can therefore lead to more accurate morphometry, and correct topological analysis. Finally, 3D imaging can often result in faster and more convenient sampling of tissue for large-scale studies.

A particular emphasis of this chapter is *automated* 3D image analysis. This term is understood to imply that the amount of manual image analysis is minimal, typically in the 0% to 10% range. These methods are distinct from manual methods, whether or not computer assistance is involved. In other words, computer-assisted methods are not considered to be automated. For example, sophisticated software/hardware packages are available for tracing neuronal processes using a computer pointing device such as a tablet or mouse (Capowski, 1989; Glaser and Glaser, 1990). Often, these packages are enhanced with visualization tools such as stereo projections and devices such as the camera lucida (Glaser and Glaser, 1990; Marko and Leith, 1992). These are examples of computer-assisted, but not automated, image analysis. Computer-assisted methods are very appropriate when a small number of images need to be analyzed, or if the complexity of the scene is too high for successful automated analysis. On the other hand, there are software packages available that accept the 3D digital image file as input, and generate as output another computer file representing a tracing of the neuron (Al-Kofahi *et al*., 2002). This output may require modest amounts of oversight and/or editing. This latter type of software is appropriately termed automated and is needed when a large number of images must be analyzed.

Stereology is an important class of computer-assisted image analysis methods (Howard and Reed, 1998; Russ and DeHoff, 2000; Mouiton, 2002). In these methods, the manual observer performs a systematic subsampling of the image data using statistically motivated rules and assumptions. For example, it is assumed that the tissue of interest has certain uniformity properties. In contrast, the methods of interest in this chapter are designed to analyze *each and every* object in a given image, without assumptions.

Although manual image analysis methods are, in principle, far more powerful than automated methods, due to the inherent superiority of the human visual system over any algorithm, there are many reasons for seeking highly automated methods. While the human visual observer excels at pattern recognition/classification tasks, s/he is often poor at detailed scoring tasks. It is common for the human observer to miss objects, score objects twice, and produce unsteady traces (Jaeger, 2000; Al-Kofahi *et al*., 2002). Indeed, it is common for the same observer to produce different

Badrinath Roysam, Gang Lin, Muhammad-Amri Abdul-Karim, Omar Al-Kofahi, Khalid Al-Kofahi • Rensselaer Polytechnic Institute, Troy, New York 12180
William Shain, Donald H. Szarowski, James N. Turner • New York State Department of Health, Albany, New York 12201

 Handbook of Biological Confocal Microscopy, Third Edition, edited by James B. Pawley, Springer Science+Business Media, LLC, New York, 2006.

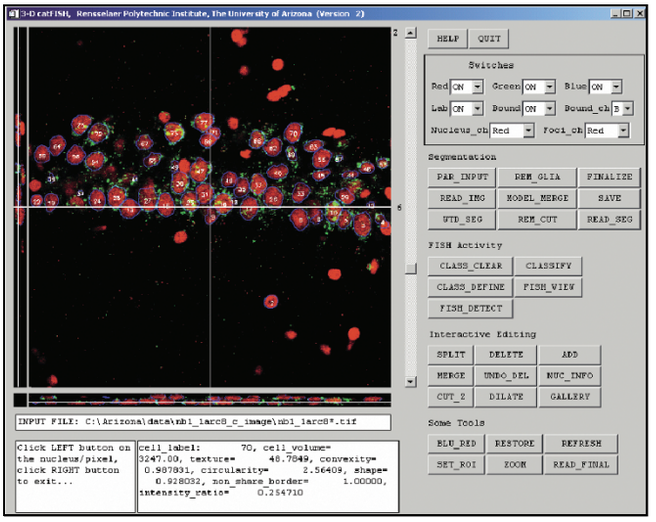

A

Nuclei					Intra-nuclear FISH			Cytoplasmic FISH		
Label	Volume	Min_Z	Max_Z	Mean-Intensity	Spot #	Spot-Score	Max-score	Area	FISH-area	Distribution (%)
1	1472	2	7	110	0	0.00	0.00	40	17	6.41
2	2251	2	8	133	0	0.00	0.00	281	2	0.07
3	2768	1	7	110	0	0.00	0.00	98	1	0.38
4	2874	4	11	126	1	2.06	2.06	332	16	4.49
5	2447	1	6	105	1	1.41	1.41	65	15	5.83
6	3351	2	8	128	0	0.00	0.00	311	19	3.74
7	4011	4	14	131	1	4.13	4.13	282	6	1.31
8	2159	2	7	93	0	0.00	0.00	71	0	0.00
9	3592	3	12	135	0	0.00	0.00	99	4	0.65
10	3563	2	11	130	0	0.00	0.00	284	10	2.63
11	2672	2	9	138	1	0.47	0.47	74	3	0.46
12	3260	2	10	136	1	0.11	0.11	328	4	0.41
13	3370	7	14	138	1	20.86	20.88	304	6	1.35
14	3857	7	14	132	5	155.79, 0.75, 0.35, 0.29, 0.09	155.79	357	89	26.45
15	3300	2	8	129	1	102.08	102.08	16	20	5.18
16	3295	2	9	130	2	9.30, 1.22	9.30	304	11	3.06
17	871	9	15	104	1	29.28	29.28	163	2	0.68
18	2591	10	16	122	3	34.27, 0.70, 0.06	34.27	31	18	4.94
19	1271	9	15	134	0	0.00	0.00	11	6	0.64
20	3808	2	10	125	2	0.13, 0.10	0.13	296	34	10.51
21	726	9	15	90	0	0.00	0.00	38	4	2.79
22	3581	3	13	136	1	4.03	4.03	280	6	1.39
23	3264	2	9	130	2	23.18, 17.07	23.18	304	27	5.33
24	2936	2	10	131	0	0.00	0.00	299	10	2.45

B

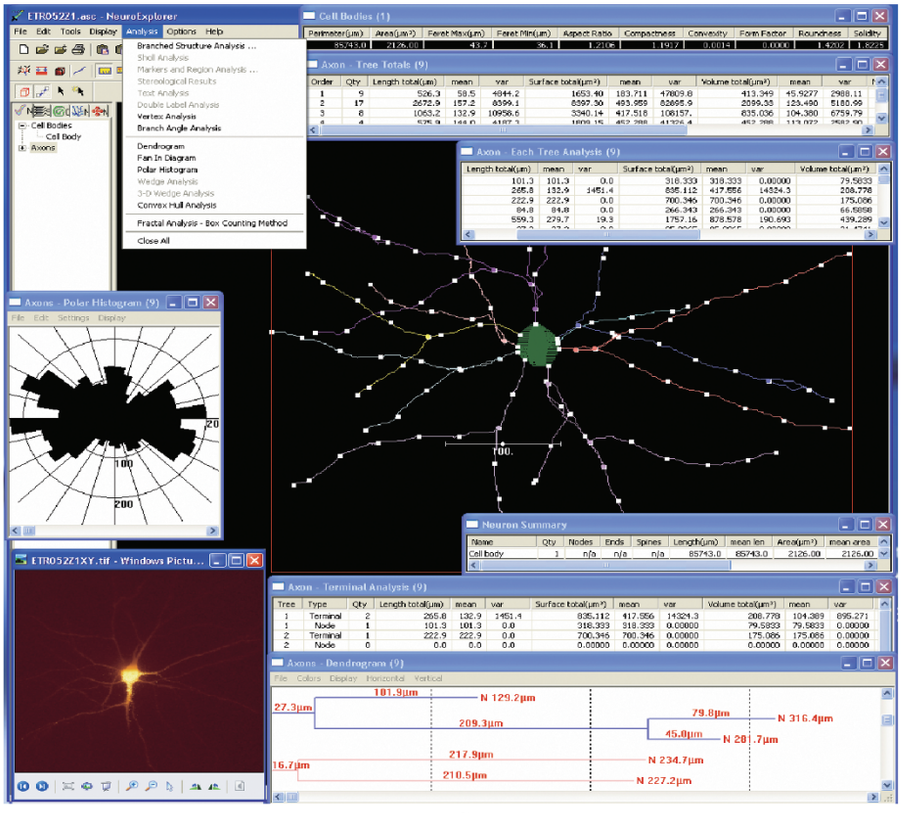

C

FIGURE 15.1. Two illustrations of 3D image analysis. In the first example (top row), confocal microscopy is used to image cell nuclei from the rat hippocampus using a DNA stain, and fluorescence *in situ* hybridization (FISH) is used to image the transcription products (mRNA) of an immediate early gene (*Arc*). The cell nuclei are segmented, and FISH activity is measured relative to the segmentation, generating a wealth of measurements. The table on the right is a partial display of the results of 3D image analysis. In the second example (lower row), a dye-injected neuron is traced automatically, generating a wealth of topological and morphological measurements displayed in tables and dendrograms (image courtesy: Microbrightfield, Inc., USA).

markups for the same image at different times. Computer automation makes sense when a large number of images must be analyzed. It can eliminate the tedium and labor associated with manual methods. It is ruthlessly consistent compared to manual methods, eliminating the subjectivity inherent to manual analysis. Faster computers make automated methods faster, and they can work round the clock.

Automated methods are free from many limitations of manual analysis. For example, manual methods are limited in their ability to process 3D data because the manual observer is limited to visual observation of stereo pairs, which are merely a projection of the 3D reality of interest. Occasionally, some observers have visual handicaps, and most observers are susceptible to optical illusions. Finally, if a study needs to be redone, it is much easier to run modified software rather than ask manual scorers to repeat a tedious task. Overall, manual methods are limited to small numbers of images, are unavoidably subjective, and are limited in the handling of three-dimensionality.

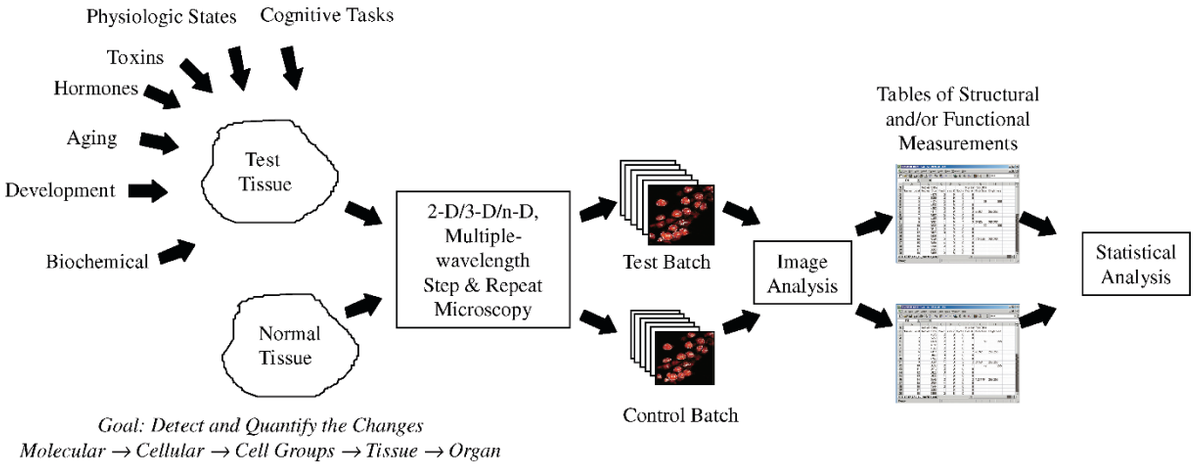

FIGURE 15.2. Illustrating the role of image analysis systems in hypothesis testing studies. Test and normal (control) tissue are imaged to generate batches of 3D images. Image analysis systems process this volumetric data to generate concise tables of measurements that are subjected to statistical analysis.

TYPES OF AUTOMATED IMAGE ANALYSIS STUDIES

Figure 15.2 illustrates the most common type of image analysis–based hypothesis testing study or assay. In this type of study, tissue samples are subjected to a condition of interest (e.g., exposed to a biochemical). As a reference, normal (untreated) tissue samples are also obtained, maintaining other conditions the same. Confocal microscopy is performed to generate batches of 3D images. Image analysis on these batches results in numerical tables representing cytometric and/or histometric data. Statistical hypothesis testing can be performed on these data. We are interested in discovery and quantification of all statistically significant differences between the treated and untreated samples. The result of hypothesis testing and an understanding of the nature of changes is a powerful source of biological insight.

Figure 15.3 illustrates a type of study that is now feasible, thanks to advances in methods and apparatus for live tissue imaging (*in vitro* or *in vivo*), as exemplified by the data in Figure 15.4. In this type of study, one collects a temporal series of images from the same region. In addition to statistical analysis of morphometric data as a function of time, it is possible to register the 3D time-series images, and identify the changes in a direct manner.

The types of changes that may be caused by the tested conditions can be diverse, and can occur at multiple levels. At the lowest level, molecular and subcellular effects can be detected by fluorescent tagging (Valeur, 2002). At the cellular level, changes can take the form of increasing/decreasing cell counts, and changes in morphometric features of cells. Finally, subtle high-level and/or long-range changes in tissue architecture can be analyzed by montaging the results of image analysis from a large number of overlapping windows across large specimens (Becker *et al*., 1996). The diversity and complexity of these changes define the breadth and scope of image analysis problems.

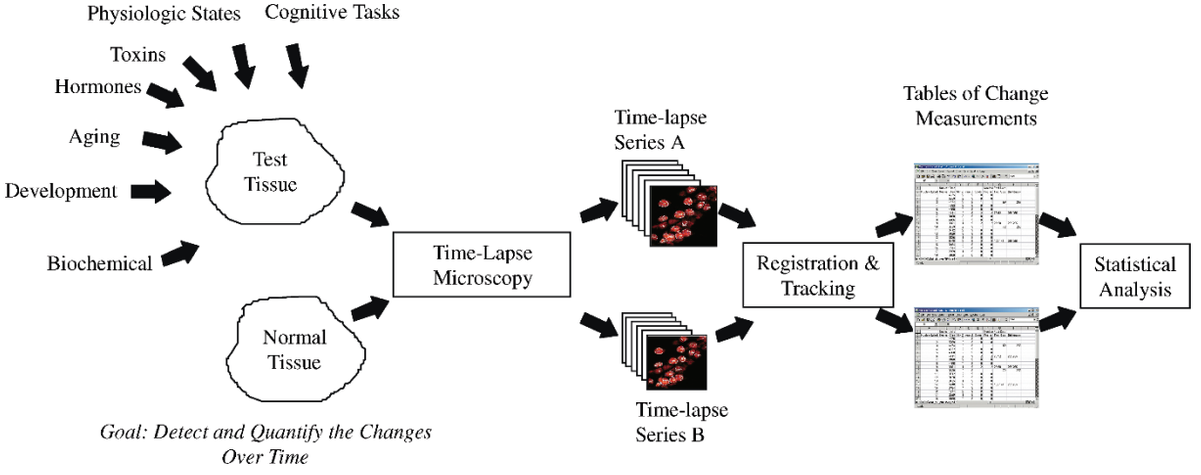

FIGURE 15.3. Illustrating the methodology for hypothesis testing with time-series data. In this case, successive images are registered (aligned) and compared. The registration algorithms usually, but not always, operate on the output of the image analysis results. Registered images (or summarized image analysis results) are compared to generate tables of change measurements that are analyzed statistically.

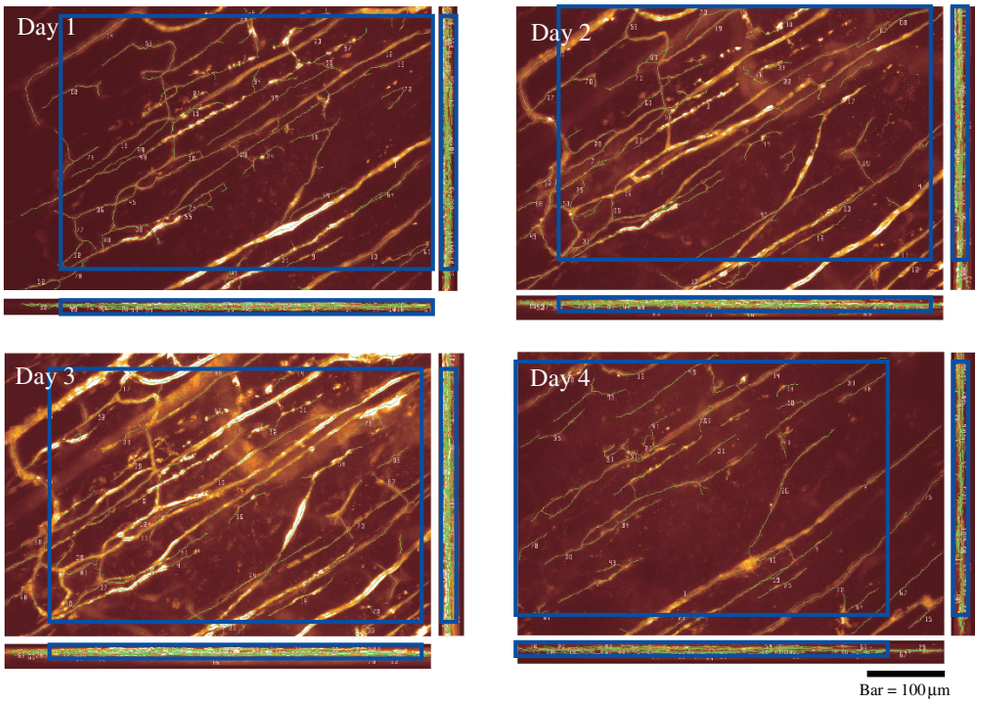

FIGURE 15.4. Time series *in vivo* images (each $768 \times 512 \times 32$, 8 bit/pixel) of fluorescently labeled skin vasculature altered by growth of a nearby tumor, shown in their maximum intensity projections (*x*-*y*, *y*-*z*, and *x*-*z*). Automated segmentation (tracing) results are overlaid in green. Volumes highlighted in blue are common overlapping regions across all images in this set of time series images, where measurements only from these common regions are used to analyze the changes in vasculature between time points. (image courtesy: Microvascular Research.)

COMMON TYPES OF BIOLOGICAL IMAGE OBJECTS

Notwithstanding the diversity of changes that may be of interest, it is advantageous to identify and study certain generic types of image objects, and common image analysis tasks associated with these object types. Practically speaking, an object is really a collection of voxels representing a biological structure imaged by the microscope. Three of the most common object types in the context of confocal microscopy are listed below.

1. **Blob-like objects**: The labeled cell nuclei in Figure 15.1(A) are examples of 3D blobs, and blobs are by far the most common type of object of interest in automated image analysis. Geometrically, they can be thought of as 3D ellipsoids that have been deformed irregularly. These apparently simple objects nevertheless provide a rich set of challenges from the standpoint of automated image analysis, due to preparation and imaging artifacts (Lin *et al*., 2003).

2. **Tube-like objects**: Vasculature and neurons [Fig. 15.1(C)] are examples of tube-like objects. Geometrically, they can be thought of as non-uniformly deformed 3D cylinders (Al-Kofahi *et al*., 2002; Abdul-Karim *et al*., 2003). Like blobs, these objects too provide a rich set of challenges for automated image analysis systems. Tube-like objects can be filled (i.e., solid) (Al-Kofahi *et al*., 2002; Abdul-Karim *et al*., 2003; He *et al*., 2003) or hollow (Weichert *et al*., 2003) in appearance.

3. **Irregular cloud-like distributions**: The diffuse FISH signals in Figure 15.1(A) are a good example of this class of object (Lin *et al*., 2003). The diversity and specificity of fluorophores, coupled with the ability of modern microscopes to image multiple fluorophores, makes this an important category of image analysis targets. Although these objects do not have distinctive geometries, they are amenable to quantitation by spatial association with biologically related blob-like or tube-like objects. For the example in Figure 15.1(A), segmentation of the nuclei provides spatial masks over which the intra-nuclear FISH signals are integrated. The extra-nuclear FISH signals are associated with the nearest nucleus by means of a Euclidean distance transformation (Lin *et al*., 2003).

SPECIMEN PREPARATION AND IMAGE PREPROCESSING METHODS

Data Collection Guidelines for Image Analysis Purposes

Specimen preparation and microscopy procedures for successful automated image analysis are stricter than for manual scoring. Unlike humans, computers are easily misled by confounding objects, artifacts, variability, and clutter. Therefore, it is important to make every effort during the specimen preparation and imaging procedures to ensure that the objects of interest are delineated with a high degree of contrast against the uninteresting structures in the tissue. It is helpful to experiment with specimen handling steps, reagents, fluorophores, and software tools such as those for spectral unmixing. Figure 15.5 illustrates structure-specific imaging using multiple fluorophores. The different highlighted structures (astrocytes, microglia, and vasculature) appear in separate image channels, eliminating the need for separating structures by image analysis. It is wise to make sure that the automated scoring software is well behaved when used on a small pilot set of images before embarking on large-scale data collection. It is important to maintain a high degree of uniformity in specimen handling, reagents, imaging protocols, and instrument settings across a batch.

Sampling conditions may be different for image analysis. For example, lossy image compression algorithms are best avoided. While image analysis algorithms are driven by the desire to maximize the accuracy of morphometry, the percentage impact of a single-voxel error depends heavily on the number of voxels representing the object. If the tissue is fairly uniform, it is often possible to sample across the tissue in a random manner, using standard stereological sampling principles (Howard and Reed,

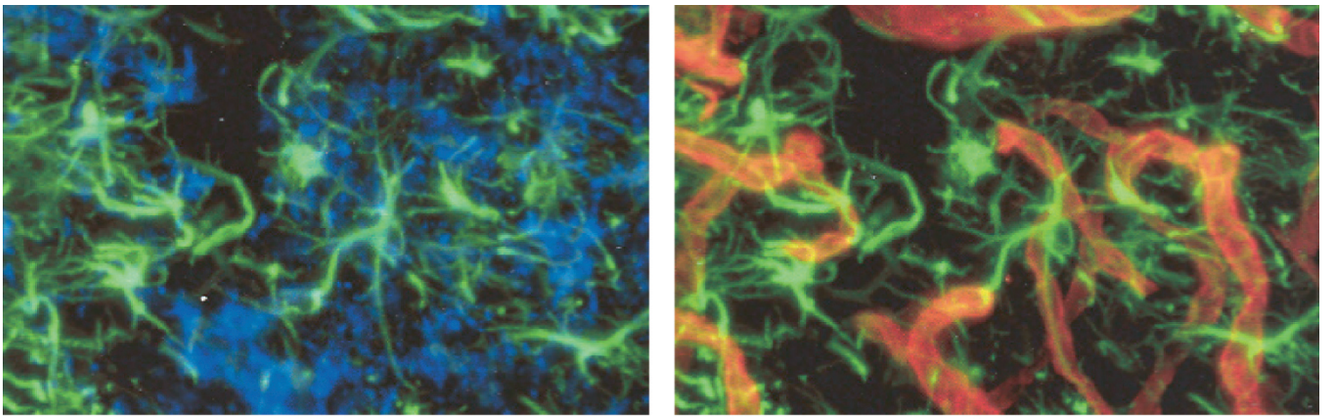

FIGURE 15.5. Neurobiology example illustrating the use of multiple fluorophores to simplify image analysis by performing selective imaging of specific structures in the same region of tissue. Maximum projections of rat cortices altered by the implantation of a model neuroprosthesis. In panel (A), the green regions represent astrocytes, the blue regions represent microglia. In panel (B), the red regions additionally represent vasculature. These different structures are available to the image analysis system as separate images. The images when compared to controls (not shown) demonstrate increased numbers of astrocytes, microglia and proliferator of vessels. (image courtesy: Dr. Beth Sipple at Wadsworth.)

1998; Russ and DeHoff, 2000; Mouton, 2002). If this assumption is not valid, it makes sense to resort to montaging. The border regions in 3D images and optical slices near the top and bottom of a stack often capture partial objects. These objects should be eliminated in a systematic manner using Howard's brick rule (Howard *et al*., 1985), which is easily implemented on the spreadsheet tables of measurements generated by the software.

If live tissue is being imaged in a time-lapse series, it is important to ensure that the same region of tissue is imaged every time (Brown *et al*., 2001). Additionally, automatic image registration tools can be used to refine the alignment (Al-Kofahi *et al*., 2003). Once registered, the changes can be quantified over the overlapping regions (Addul-Karim *et al*., 2003). Figure 15.4 shows a time series of *in vivo* images (each $768 \times 512 \times 32$, 8 bit/pixel) of fluorescently labeled vasculature of skin altered by growth of a nearby tumor.

Confocal microscopes are unavoidably anisotropic in terms of the spatial sampling density because the axial resolution of confocal microscopes is lower than the lateral resolution. Image resampling by techniques such as shape-based interpolation often simplifies 3D image analysis at the expense of generating a larger image data set (Raya and Udupa, 1990).

Finally, the image analyst must be aware that the brightness of a voxel in a confocal image is not necessarily only proportional to the fluorophore concentration (Pawley, 2000).

Image Preprocessing Methods

Common imaging artifacts include non-uniformity and the presence of uninteresting/nuisance objects. Their effects on the image analysis results can sometimes be reduced by preprocessing. Figure 15.6 shows several imaging artifacts in neuron and vasculature images.

Morphological filters (Serra and Soille, 1994; Bovik *et al*., 2001), background subtraction (Russ, 1994), and signal attenuation–correction (Adiga and Chaudhuri, 2001b; Can *et al*., 2003) are examples of common preprocessing methods for confocal images. Morphological filters, such as the median and top-hat filter, are typically utilized to reduce image noise, such as blobs of dye in the background, or to smooth out Poisson noise (Sarti *et al*., 2000) and non-uniformities of foreground intensity. However, the optimal method for removing Poisson noise is full 3D deconvolution (see Chapter 25, *this volume*). Background subtraction is performed to correct illumination non-uniformity across the entire image. Signal attenuation–correction is useful to rectify depth-

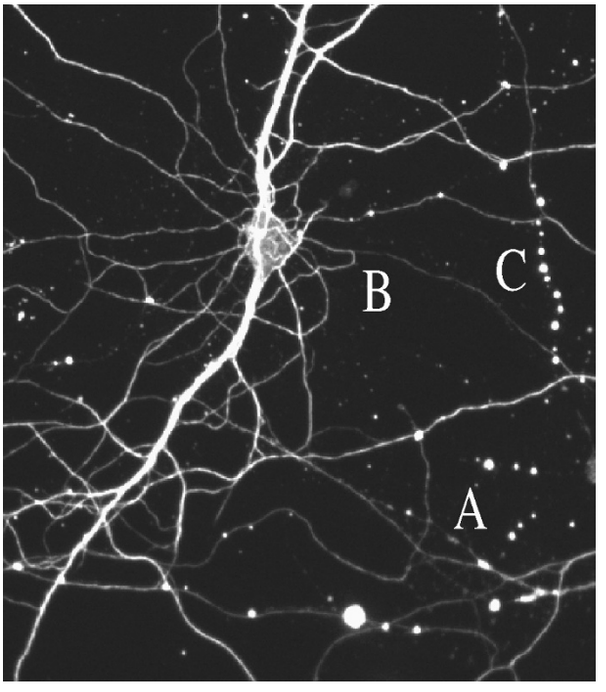

FIGURE 15.6. Examples of imaging artifacts in the context of neuron imaging. **(A)** Blobs of dye. **(B)** Neurites with relatively dim and discontinuous appearance. **(C)** Strip of noise, resembling neurites. (image courtesy: Natalie Dowell at the Wadsworth Center.)

dependent attenuation of signals (Can *et al*., 2003). In general, images are preprocessed globally, that is, without localizing the preprocessing operations to a subset of the image. This makes preprocessing computationally expensive. Furthermore, the preprocessor parameters usually need to be fine-tuned to ensure preservation of objects of interest while reducing unwanted artifacts.

Another rationale to preprocessing is to generate standardized images where one segmentation method is used for images coming from different sources. Yet another is to highlight particular structures, for example, images of neuronal processes and vasculature may be preprocessed to highlight the tube-like morphology of these biological objects (Sato *et al*., 1998).

GENERAL SEGMENTATION METHODS APPLICABLE TO CONFOCAL DATA

Segmentation is the process of labeling some or all of the voxels in the image as being part of specific objects of interest (the **foreground**) and not part of the **background**. This is the process of transitioning from a conceptually simple array of point measurements (voxels) to the more abstract and more informative notion of image objects, or parts thereof (Haralick and Shapiro, 1985). Following segmentation, it is straightforward to make morphological and functional measurements. The purpose of this section is to summarize the main segmentation approaches. The reader interested in more detailed descriptions is referred to other sources (Bhanu, 1982; Wilson and Spann, 1988; Bhanu and Lee, 1994; More and Solimini, 1995; Rezaee, 1998; Suri *et al*., 2002).

The difficulty of segmenting biological images is largely attributable to their sheer complexity and variability. Interestingly, it is simpler to segment 3D images, compared to 2D images because, in the former, some overlapping objects can be distinguished on the basis of 3D depth information (Ancin *et al*., 1996).

The prior literature on segmentation is vast (Zucker, 1977; Kanade, 1978; Sklansky, 1978; Rosenfeld and Davis, 1979; Ranade and Prewitt, 1980; Fu and Mui, 1981; di Zenzo, 1983; Haralick and Shapiro, 1985; Mitiche and Aggarwal, 1985; Nevatia, 1986; Cooper, 1998; Kerfoot and Bresler, 1999; Pham *et al*., 2000). Generally, techniques for image segmentation can be grouped into three categories: bottom-up methods, top-down methods, and hybrid methods. Regions and boundaries are two common concepts commonly used in segmentation. Intuitively, an **object** is outlined by its boundary and a **region** is contained by a boundary. In addition, segmentation may be performed either image wide, or in an exploratory manner. Non-exploratory methods visit each voxel and label them. Exploratory methods (Can *et al*., 1999; Al-Kofahi *et al*., 2002; Streekstra and van Pelt, 2002; Abdul-Karim *et al*., 2003) begin with voxels known or estimated to be on the object, such as a point on a vessel, and proceed to segment adjacent voxels of the same object.

Bottom-Up Segmentation Methods

Bottom-up methods start with an over-segmentation of the image and iteratively merge object fragments based on some measure of similarity. They can be described in terms of three steps: identifying the set of initial regions representing object fragments (Zucker, 1976; Besl and Jain, 1988; Adams and Bischof, 1994; Trucco and Fisher, 1995; Zhu and Yuille, 1996), identifying an appropriate region-similarity measure (Blake and Zisserman, 1987; Black and Rangarajan, 1996), and merging the voxels that share these features into objects (Guigues *et al*., 2003). Other related methods are graph based, for example, the work of Shi and colleagues (Beck *et al*., 2000) has presented a global criterion termed the "normalized cut" for segmenting the graph. Ying and Uberbacher (1997) proposed a 2D image segmentation using a minimum spanning tree partitioning approach. In the bottom-up category, there are four main approaches: intensity thresholding, region based, boundary based, and integrated techniques. These are detailed in the following paragraphs.

Intensity Threshold–Based Segmentation Methods

In this approach (Sahoo *et al*., 1988), all voxels whose values lie within a certain range belong to one class. *Global thresholding* (Shapiro and Stockman, 2001; Koh *et al*., 2002) uses a single threshold value for an entire image. When the threshold value changes for different regions of the image, it is called *adaptive thresholding* (Cohen *et al*., 1994; Kim *et al*., 2001; He *et al*., 2003). Thresholding may be sufficient for segmentation when the background intensity range does not overlap with the foreground intensity range. To overcome the limitations of thresholding, such as susceptibility to background noise and intensity non-uniformity, *connected components analysis* (Dillencourt *et al*., 1992; Ancin *et al*., 1996) is commonly used to link voxels belonging to an object of interest, and reject overly small clusters of pixels.

Region-Based Segmentation Methods

Region-based methods (Zucker, 1996; Hojjatoleslani and Kittler, 1998) rely on the assumption that neighboring voxels within one region of an object are homogeneous according to a specified measure. This leads to a class of algorithms known as split-and-merge (Horowitz and Pavlidis, 1974; Haralick and Shapiro, 1985; Chang and Li, 1994), seeded region growing (Adams and Bischof, 1994; Hojjatoleslami and Kittler, 1998), and partitional clustering (Mackin *et al*., 1993; Roysam *et al*., 1994). The general procedure is to compare each voxel to its neighbors. If the criterion of homogeneity is satisfied, the voxel is said to belong to the same class. Neighboring voxels are examined and added to the region if they are evaluated to have similar characteristics. This region growing process will eventually converge, yielding a delineation of the object. The growing volume should be constrained for maximum success. Multiple regions can be initialized in the image, and regions can be merged with each other. Obviously, the performance of this approach largely depends on the selected homogeneity criterion.

In the split-and-merge technique, the entire image is initially considered as one region. In each step, each heterogeneous region of the image is divided into four rectangular segments and the process is terminated when all regions are homogeneous. After the splitting, a merging process unifies the similar neighboring regions. Quadtree-structured split-and-merge (Pavlidis, 1977) is a popular approach because of its simplicity and computational efficiency. Seeded region growing techniques (Adams and Bischof, 1994; Hojjatoleslami and Kittler, 1998) select some initial image points, and then segments the image into regions, each originating with a single seed. Clustering-based methods (Mackin *et al*., 1993; Roysam *et al*., 1993, 1994) treat the segmentation problem as a partitional cluster analysis (Theodoridis and Koutroumbas, 1999) in a four-dimensional space $[(x, y, z), I(x, y, z)]$, combining the usual spatial coordinates with the image intensity. This approach is most valuable when the available geometric information about the objects is weak (Shain *et al*., 1999).

Boundary-Based Segmentation Methods

Boundary-based methods (Davis, 1975) detect image edges (Ballard and Brown, 1982), and link them into contours/surfaces representing object boundaries. The output of most existing edge detectors can only provide candidates for the region boundaries because the edges obtained are normally discontinuous or over-detected. However, the actual region boundaries should be closed curves. Therefore, some postprocessing, such as edge tracking, gap filling, smoothing, and thinning should be performed to obtain the closed region boundaries. Such postprocessing is often problematic, and this is an inherent limitation of boundary-based methods (Shapiro and Stockman, 2001).

Integrated Segmentation Methods

Integrated methods combine boundary and region criteria. In this class of methods, the morphological watershed algorithm is widely studied and used for efficient object separation (Beucher, 1991; Dougherty, 1993; Vincent, 1993; Serra and Soille, 1994; Shafarenko *et al*., 1997). Introduced by Digabel and Lantuejoul (1978), extended by Beucher (1982), analyzed theoretically by Maisonneuve (1982), and formally defined in terms of flooding simulations by Vincent and Soille (1991), the term "watershed" comes from a graphic analogy attributed to Vincent and Soille. In this analogy, the gray level image is treated as a topographic intensity surface. It is assumed that holes have been punched in each valley bottom. If this surface is "flooded" from these holes, the water will progressively flood the catchment basins (set of surface points whose steepest slope paths reach a given minimum) of the image. At the end of this flooding procedure, each minimum is completely surrounded by "dams," which delimit its associated "catchment basins." The set of dams obtained in this way corresponds to watersheds (called the watershed surface in 3D case) from a geophysical analogy, and provides a tessellation of the input image into its different catchment basins. Unlike the boundary-based methods above, the watershed is guaranteed to produce closed boundaries even if the transitions between regions are of variable strength or sharpness. Its popularity is also attributable to its computational efficiency and extendability to 3D spaces (Higgins and Ojard, 1993; Sijbers *et al*., 1997).

The second method in the class is variable-order surface fitting (Besl and Jain, 1988) that starts with a coarse segmentation of the image into several surface-curvature-sign primitives (e.g., pit, peak, ridge, etc.) which are refined by an iterative region-growing method based on variable-order surface fitting.

Another method in the class is to integrate region-growing and edge-detection (Pavlidis and Liow, 1990). This starts with a split-and-merge algorithm, and eliminates or modifies region boundaries based on some criterion using boundary smoothness and the variation of image gradients. Haddon and Boyce (1993) generate regions by partitioning the image co-occurrence matrix and then refining them by relaxation using edge information.

Top-Down Segmentation Methods

Unlike bottom-up algorithms, such as those described in the previous section, which are based on low-level image-based cues, such as coherence of brightness, color, texture or motion, top-down methods rely on prior models for the objects in the image to carry out the segmentation. Even sophisticated pre- and postprocessing techniques cannot overcome the inherent limitations of purely intensity-based methods. Actually, for automatic object segmentation, some kind of prior related knowledge can and must be incorporated into the algorithms. The mid- and high-level knowledge must be used to either confirm or modify the initial segmentation. This leads to the top-down approach, where the segmentation is guided by some known representation or prior knowledge of the objects under study. One method in this class is model-based segmentation, which optimizes the fit between a model and the image data. Different procedures, such as *deformable shape models* (Cootes *et al*., 1995; McInerney and Terzopoulos, 1996; Lorigo *et al*., 2001; Ghanei and Soltanian-Zadeh, 2002) and *statistical models* (Vemuri and Radisavljevic, 1994; Staib and Duncan, 1996), have been proposed. Deformable models, also known as "*snakes*" or "*active contours*," have been used as a way to incorporate application-specific *a priori* knowledge. For example, in order to segment a bone in a medical image or in order to visually track a person, models describing the possible contours of the objects of interest are used. The parameters of the models specify object properties such as the pose, size, and shape. Sunil Kumar and Desai (1999) presented a method of joint segmentation and image interpretation. Neumann (2003) proposed a knowledge-guided segmentation in 3D imagery. Statistical shape modeling methods depend upon the availability of parametric models to describe the objects. These parameters must be selected carefully in order to accurately characterize the objects, and discriminate outliers from real objects in an effective manner. The set of parameters must be rich enough to describe complex objects.

Although top-down methods are appealing because they seem similar to the human cognitive process, they have the disadvantage that they require a large amount of *a priori* knowledge (e.g., object models, number of regions) and this tends to limit the scope of applicability.

Hybrid Segmentation Methods Combining Bottom-Up and Top-Down Processing

Both top-down and bottom-up methods have their advantages and disadvantages. The latest segmentation methods often combine both low-level and high-level approaches (Roysam *et al*., 1992; Roysam and Miller, 1992; Bhattacharjya and Roysam, 1994). However, as these approaches tend to be computationally intensive and overly specialized, they are not described in further detail here. More pragmatic approaches do exist. One such is described in the following section.

EXAMPLE ILLUSTRATING BLOB SEGMENTATION

Accurate, reliable, and highly automated segmentation of fluorescently labeled cell nuclei from 3D confocal images is an essential first step for quantification by association of various genomic and proteomic products in nuclear or cytoplasmic compartments [Fig. 15.1(A)]. Tightly packed cell layers, which often result in the appearance of "touching objects" in image stacks, is a common segmentation problem. Precise segmentation of nuclei is an absolute requirement for correct assignment of gene transcription products to nuclear versus cytoplasmic locations for achieving optimal temporal resolution (Lin *et al*., 2003).

Lin and colleagues (2003, 2004) described an algorithm that uses a statistical model-based approach to combine the attractive

features of the 3D watershed algorithm, with algorithms that exploit available intensity-gradient–based cues, and the knowledge of the expected anatomic shape of the object. Whenever the cell shapes are well defined, the best-available methods for separating touching objects are based on the watershed algorithm (Ancin *et al*., 1996; Lin *et al*., 2003). When the cell shapes are poorly defined, partitional cluster-analysis algorithms work better (Roysam *et al*., 1994).

The watershed algorithm is widely studied and used for efficient object separation (Vincent and Soille, 1991; Ancin *et al*., 1996; Malpica *et al*., 1997; Solorzano and Rodriguez, 1999). Notwithstanding its popularity, watershed algorithm has several limitations arising from the fact that it relies on touching objects exhibiting a narrow "neck" in the region of contact. These necklines play a critical early role in estimating the number of objects in a given cluster, and is notoriously error prone. Considerable effort has been devoted to the design of algorithms for generating the correct set of "geometric markers" to guide the object segmentation. The problem of determining the correct number of such markers is inherently a difficult one, and is conceptually similar to the problem of automatically determining the number of groups in multi-dimensional statistical data. To overcome the above difficulties, Lin and colleagues (2003) proposed a "*gradient-weighted distance transform*," that combines object separation hints derived from geometric and intensity cues in the image data to improve watershed segmentation. Specifically, the geometric-distance transform **D** (Borgefors, 1986) and the gradient transform **G** (Lin *et al*., 2003) are combined into a single representation that captures the object separation cues available in the data, as given by the following formula.

$$\mathbf{D}' = \mathbf{D} \times \exp\left(1 - \frac{\mathbf{G} - G_{\min}}{G_{\max} - G_{\min}}\right),$$

where $G_{\min}$ and $G_{\max}$ are the minimum and maximum values of the gradient **G** needed for normalization. It is easy to observe that the modified distance value **D′**, has a high value at positions closer to the center of foreground objects, and for voxels with smaller gradient values. It has smaller values close to the boundary of the foreground objects, or where the gradient is relatively large. This expresses the object separation cue that the voxels with bigger gradient values tend to lie on the boundary of an object. In practice, the watershed algorithm requires the inverse of this distance transformation. This inverse is denoted **T**, and is computed as follows:

$$\mathbf{T} = S_g(\max(\mathbf{D}') - \mathbf{D}'),$$

where max(**D′**) is the global maximum within the distance images, and S_g represents a Gaussian smoothing operator (Castleman, 1996). The smoothing operation is needed because the transformed image may contain tiny noise-caused intensity peaks, usually due to uneven cell staining. Figure 15.7 illustrates the effectiveness of the combined measure. Panel (A) shows a sample image, with the nuclei indicated in blue, and the FISH signal displayed in red. Panel (B) is a surface plot of the geometric distance **D** for the region indicated by the white box in (A). Panel (C) is the result of combining the geometric and gradient measures **D** and **G** above. It is clear that the combined transformation in Panel (E) is effective in discriminating this touching nuclear cluster even though it does not have the characteristic bottleneck-shaped connection pattern.

Model-Based Object Merging

Although the gradient-weighted distance transform described above essentially eliminates under-segmentation, the problem of over-segmentation remains. To correct the over-segmentation, it is necessary to detect and break (eliminate) false watershed surfaces and thereby merge cell objects (Adiga amd Chaudhuri, 2001a; Lin

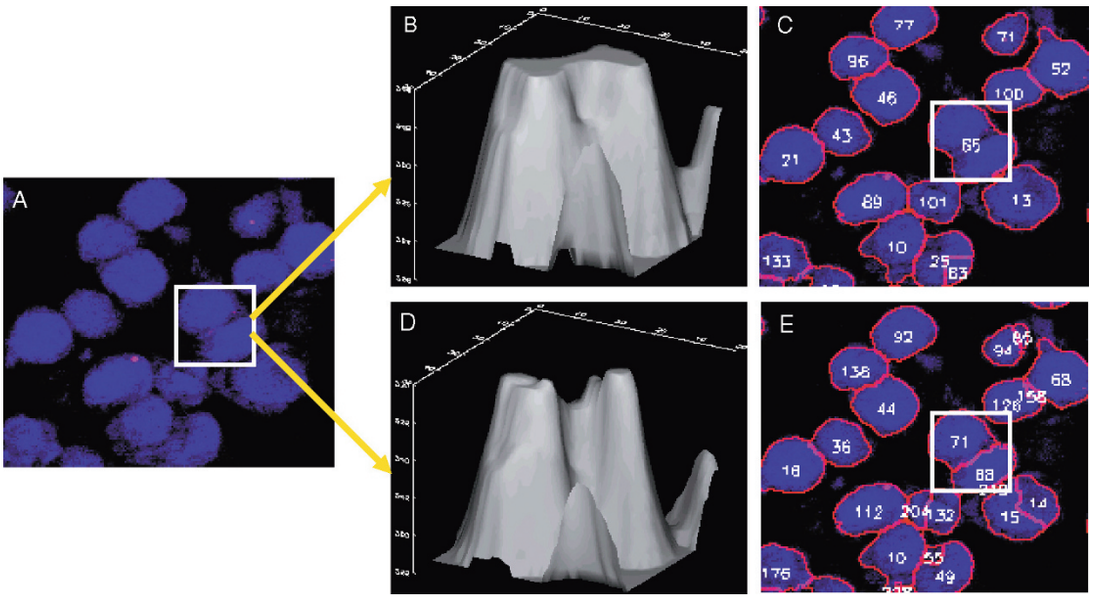

FIGURE 15.7. Illustrating the combined gradient-weighted distance transform as a cue of separating connected objects. (A) A small portion of a 3-D confocal image stack, showing nuclei in the *CA1* region of a rat brain. The white box in panel (A) indicates the region of interest, which includes two touching nuclei. Panel (B) shows a surface plot showing a standard geometric distance map ***D*** which is not adequate for nuclei separation. The combined gradient-weighted distance map in panel (D) results in the correct segmentation shown in panel (E). (Courtesy: Journal of Cytometry.)

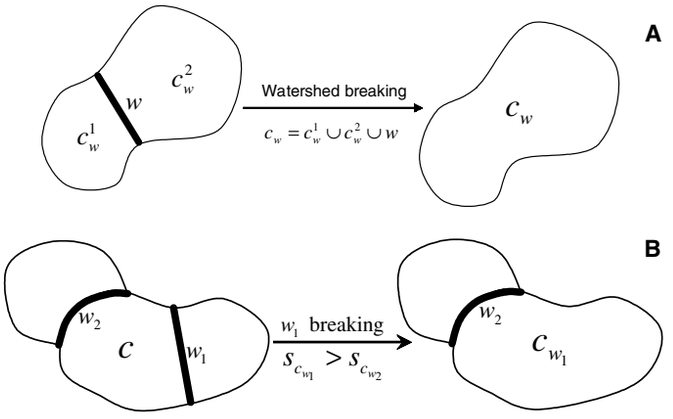

FIGURE 15.8. Illustrating two example cases encountered by the watershed surface-breaking algorithm for touching objects. Panel (A) shows a case that leads to merging of the two objects. Panel (B) shows the case that one object has multiple watershed surfaces (two in this example). In this case, there are two candidate watershed surfaces to choose from for breaking. The watershed surface w that has a greater merging score C_w is given the higher priority, indicating better fit to the object model, thus the higher confidence towards its breaking. (Courtesy: Journal of Cytometry.)

et al., 2003). Currently, the best methods rely on a quantitative score based on a mathematical model of the objects of interest (i.e., the nuclei). The object model is described by a vector of features that are denoted as X_c for object (cell nucleus) c. The features include measurements such as volume, texture, convexity, circularity, and shape. The merging score based on these features is given below assuming that they are Gaussian-distributed:

$$\mathbf{T} = S_g(\max(\mathbf{D}') - \mathbf{D}'),$$

where $\bar{X}$ and Σ_X are the mean and covariance matrix of the training feature set respectively, which are obtained from some example intact nuclei in the given image stack.

Intuitively, the merging decisions are based on the following two criteria: (i) the merging score S_{cw}, that is, the score of the combined object by nucleus c_w^1, c_w^2, and watershed surface w should be higher than the score of either nucleus S_{cw}^1 or S_{cw}^2 before merging. (ii) The gradient of watershed surface w should be relatively large compared with the gradient of the nucleus c_w^1 and c_w^2. It is assumed that intranuclear gradients are smaller than internuclear gradients. With these observations in mind, the following ratios are calculated:

$$R_{s_w} = \frac{2 \times S_{c_w}}{\left(S_{c_w^1} + S_{c_w^2}\right)};$$

$$R_{\gamma_w} = \frac{\left(\gamma_{c_w^1} + \gamma_{c_w^2}\right)}{2 \times \gamma_w}.$$

The final decision-making criterion is the combination of the above two ratios:

$$R_w = R_{s_w} \times R_{\gamma_w} \geq \beta,$$

where β is an empirically set decision threshold. Further details concerning the above algorithms are provided in Lin and colleagues (2003). Figure 15.8 illustrates two example cases encountered by the watershed surface-breaking algorithm for touching objects. The model-based watershed surface breaker effectively eliminates almost all of these over-segmented nuclei during the postprocessing. One example is shown in Figure 15.9, where the above algorithm achieves a 97% accuracy compared to a consensus of three expert observers.

EXAMPLE ILLUSTRATING SEGMENTATION OF TUBE-LIKE OBJECTS

Two broad types of algorithms exist for segmenting tube-like objects (neurons, vasculature): (i) skeletonization and (ii) vectorization. Skeletonization methods work by systematically eroding a binarized version (the results of adaptive thresholding) of the image until only the innermost voxels (i.e., the skeleton) remains. They are attractive for applications in which the objects are irregular, for example, spiny neurons (Koh *et al*., 2002). On the other hand, vectorization-based methods are valuable when the objects are much more regular in appearance, and can be modeled as generalized cylinders in 3D space (Al-Kofahi *et al*., 2002; Abdul-Karim *et al*., 2003, 2005). The latter method embeds more assumptions about the objects of interest, and is therefore better at rejecting image clutter than skeletonization-based methods. Figure 15.10 shows an example of skeletonization results (Koh *et al*., 2002; He *et al*., 2003) and Figure 15.11 exemplifies vectorization results (Al-Kofahi *et al*., 2002), both on dye-injected neurons imaged by a confocal microscope.

Skeletonization Methods

These methods work by performing adaptive segmentation (producing a binary image) followed by skeletonization and graph extraction (Koh *et al*., 2002; He *et al*., 2003). The 3D skeleton of an object is a connected set of lines (traces) that coincide with its medial axis, and which can be obtained by repeatedly performing erosion operations and connectivity analysis on the 3D binary volume, until only the medial skeleton of the object remains. During the thinning process, a voxel is considered deletable if its removal does not cause any other voxels to become disconnected. Clearly, improved detection of voxel connectivity allows more voxels to be deleted, and hence a more concise skeleton can be obtained. The traditional methods (Tsao and Fu, 1981; Gong and Bertrand, 1990) for 3D skeletonization are based on analyzing a $3 \times 3 \times 3$ window around each voxel to test for voxel deletability. One drawback of such methods is their inability to detect many cases when voxels are connected via more circuitous paths, especially in noisy data such as that from confocal microscopy. Specifically, these algorithms can magnify each of the however-small noise-caused surface irregularities into full skeletal appendages, resulting in an excessively complex skeleton. Cohen and colleagues (1994) developed a thinning algorithm based on performing voxel detability tests over windows much larger than $3 \times 3 \times 3$, and using long-range boundary detection criteria (He *et al*., 2003).

Vectorization Methods

In contrast, vectorization methods utilize a more rigid model that embeds tighter assumptions about the objects. For example, it often explicitly models tube-like objects geometrically, say using a generalized cylinder constrained by parallel boundaries (Al-Kofani *et al*., 2002) (Fig. 15.12). Figure 15.4 illustrates an example of tracing tumor microvasculature using a semi-rigid

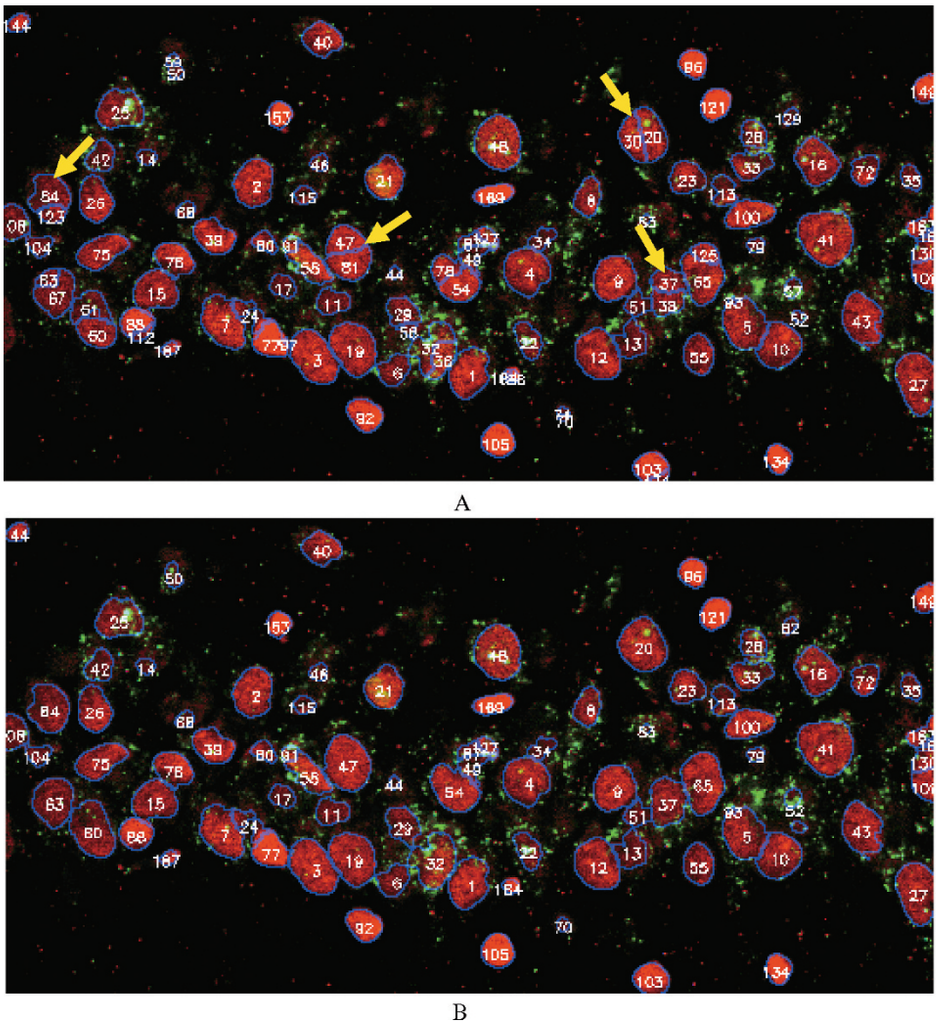

FIGURE 15.9. Segmentation result generated by the model-based merging procedure (i.e., the watershed surface breaker). There were 66 watershed surfaces broken, and most cases of over-segmentation were eliminated. An explicit mathematical model for the anatomic characteristics of cell nuclei, such as size, texture, convexity and shape measures, is incorporated during the post-merging procedure. Panel (A) shows the segmentation right after the enhanced watershed algorithm. As can be seen, clusters of nuclei are basically eliminated, and the over-segmentation is allowed, as indicated by yellow arrows. Panel (B) shows the final results after the model-based merging procedure. (Data courtesy: Carol Barnes Lab at the University of Arizona.)

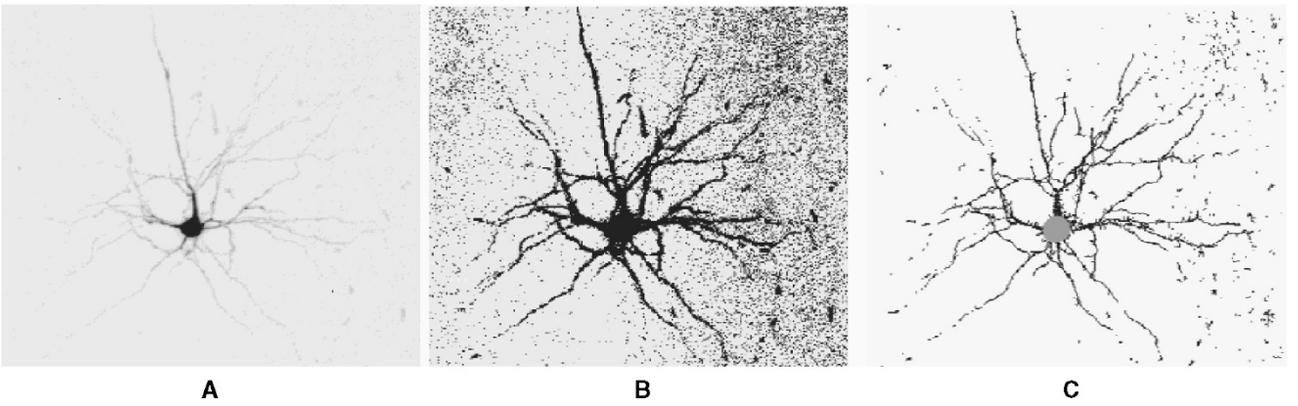

FIGURE 15.10. Illustrating neuron tracing by skeletonization. (A) 3-D image of a dye-injected neuron, shown in maximum-intensity projection (8-bit/voxel, $383 \times 328 \times 150$). (B) Segmented image by adaptive thresholding. (C) Skeletonized neuronal process shown with the detected soma. The skeletonization method is very general, so it can apply to spines, for example, but it is not nearly as fast and selective as the vectorization method. (image courtesy: Microscopy and Microanalysis.)

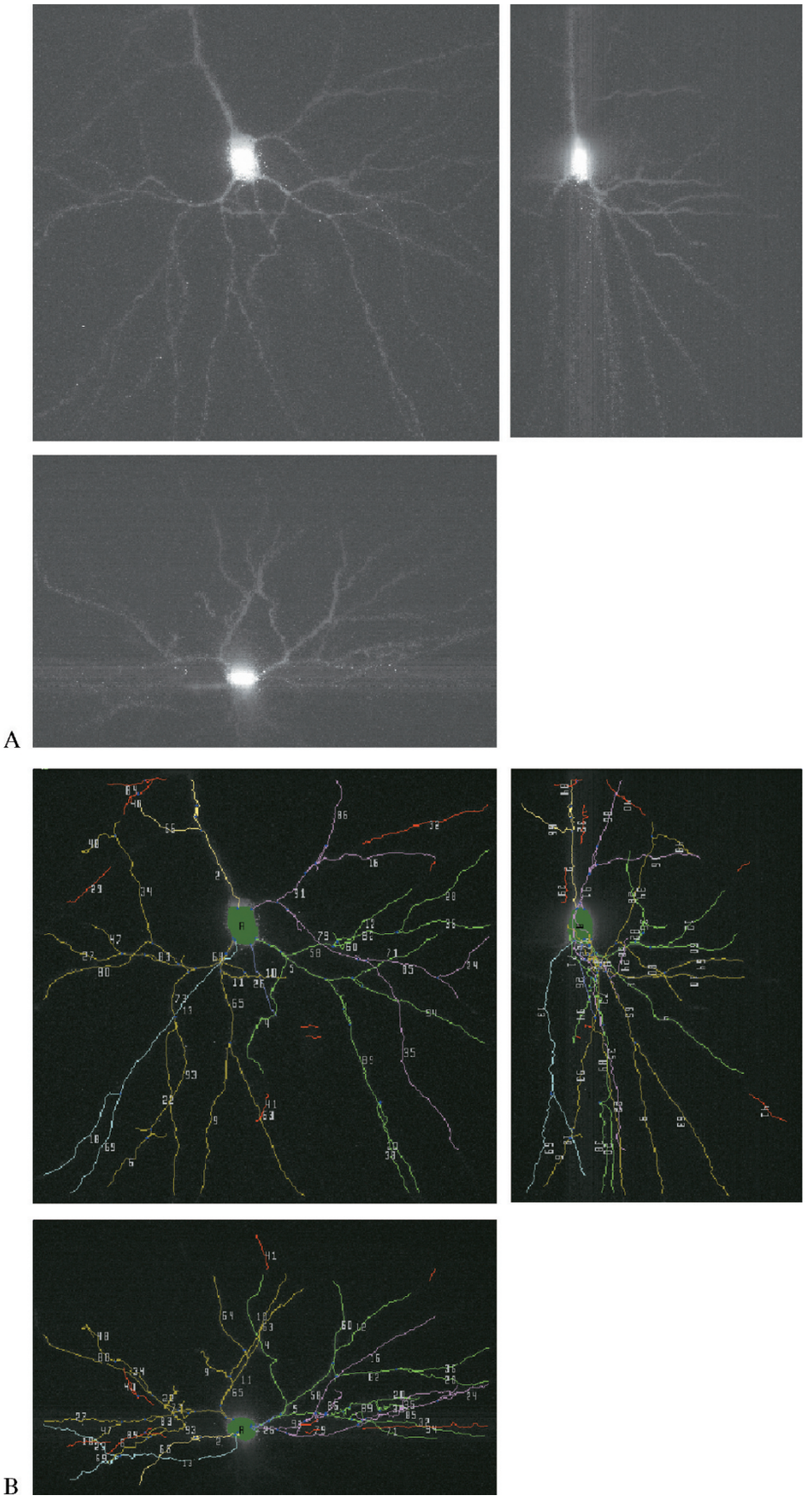

FIGURE 15.11. Illustrating neuron tracing using a generalized cylinder model and vectorization. (A) A 3-D, $512 \times 480 \times 301$ grayscale image of a dye-injected neuron shown by the *x-y*, *x-z*, and *y-z* maximum intensity projections. (B) The segmentation results using a rigid, generalized cylinder model. Notice that since the segmentation is guided using a spatio-physical model, no background voxels are misclassified since they do not fit the generalized cylinder model. This approach can be much more selective than the skeletonization method and substantially faster. However, it is not as effective at segmenting non-tube-like structures such as spines.

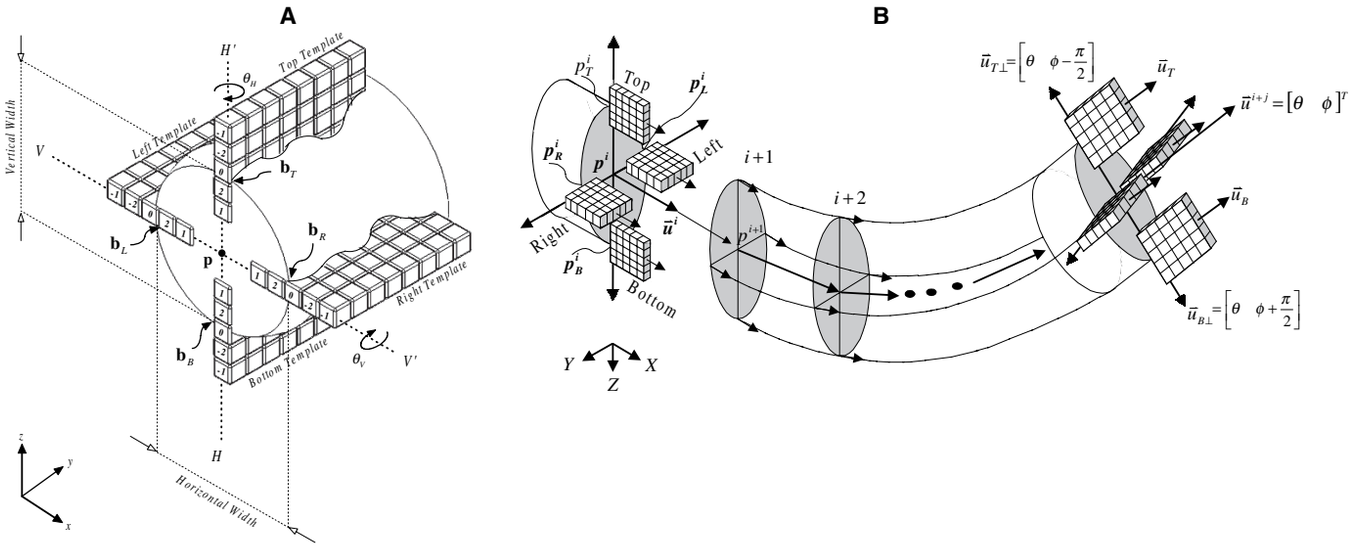

FIGURE 15.12. (A) Modeling a tube-like object using a generalized cylinder. Irregularities of the object boundary relative to the straight-boundary assumption are incorporated into the model. (B) Illustrates the recursive exploratory tracing (vectorization) of a tube-like structure, advancing with the information gathered from best-fit cylinder at each point. (pictures courtesy: Microvascular Research, IEEE Press.)

model. The following paragraphs describe the core ideas in further detail.

At the simplest level, tube-like structures can be modeled as piecewise-linear segments, where each segment is a generalized cylinder (Al-Kofahi *et al*., 2002). The key geometric property is the existence of anti-parallel edges located a small distance apart. Even this apparently simplistic modeling leads to a highly successful analysis exemplified by Figure 15.11. In practice, the strict cylinder model is relaxed to account for slight irregularities in the vasculature boundaries [Fig. 15.12(A)] by incorporating a tolerance to deviations from the strict cylinder model in the software implementation. Often, the structures of interest are much more irregular, as exemplified by the tumor microvasculature in Figure 15.4. This irregularity can be modeled by the use of robust statistics, which implies the use of a median instead of the arithmetic mean (Abdul-Karim *et al*., 2003). This method is described below, and illustrated diagrammatically in Figure 15.12(B).

At the core of this method is the estimation of boundary locations and direction. The estimation utilized directional edge detectors, called templates, comprised of linearly stacked one-dimensional (1D) edge detectors (Sun *et al*., 1995) of the form $[-1, -2, 0, 2, 1]^T$ along a direction. Along a particular direction, the edge strengths from each 1D edge detector are averaged [using mean (Al-Kofahi *et al*., 2002) or median (Abdul-Karim *et al*., 2003)] and the resulting value is associated with the corresponding template, referred to as a *template response*. This can be expressed mathematically as

$$(\mathbf{b}^i, \mathbf{u}^i, k^i) = \underset{\left\{(\mathbf{b},\mathbf{u},K)\,|\,\mathbf{b}=\mathbf{p}^i+m\mathbf{u}_\perp,\, m=1,\ldots,\frac{M}{2},\, \mathbf{u}\in\mathbf{U},\, k\in K\right\}}{\arg\max} [R(\mathbf{b}, \mathbf{u}, K)],$$

where $\mathbf{U}$ is the set of unit vectors along directions in the neighborhood of $\mathbf{u}^i$ and K is the set of all template lengths. The vector $\mathbf{u}$ is a unit vector along a particular 3D angle θ, while $\mathbf{u}_\perp$ is the unit vector perpendicular to $\mathbf{u}$. The parameter M is the user-defined diameter of the widest expected vasculature. Values $\mathbf{b}^i$, $\mathbf{u}^i$, k^i are the results of this exhaustive search at iteration i, each representing the $[x, y, z]$ location, orientation, and length, respectively, of the template that returns the maximum response R. This search is performed four times corresponding to the four templates that make up the generalized cylinder model [Fig. 15.12(A)]. The corresponding mean and median template response, respectively, are expressed as

$$R(\mathbf{b}, \mathbf{u}, K) = \underset{k\in K}{\arg\max} \{\underset{j=1..K}{median}(r(\mathbf{b}+j\mathbf{u}, \mathbf{u}_\perp))\},$$

and

$$R(\mathbf{b}, \mathbf{u}, K) = \underset{k\in K}{\arg\max} \left\{\frac{1}{k}\sum_{j=1}^{k}(r(\mathbf{b}+j\mathbf{u}, \mathbf{u}_\perp))\right\},$$

where $r(\mathbf{b},\mathbf{u}_\perp)$ is the response of a single 1D edge detector at $\mathbf{b}$ along the direction that is perpendicular to $\mathbf{u}$. Notice that a template of length k is comprised of k 1D edge detectors stacked together, hence, r is essentially a template of length 1. The simple switch from mean to median averaging deserves a closer inspection. By using the median, the response function is robust to at most 50% of outliers (Huber, 1981), loosely termed as *bad edges*. Figure 15.13 further demonstrates the difference between these two averaging methods.

Notice that by using this rigid model both the centerline and boundary are readily obtained while segmenting the image, yielding morphometrics such as length (cumulative distance between center points) and diameter (distance between boundary points) on the fly. In contrast, the skeletonization approach requires much more sophisticated postprocessing to extract these morphometrics. In either case, additional processing must be performed for branch analysis and to extract any other morphometrics from the segmented structure. Details of this method are described elsewhere (Al-Kofahi *et al*., 2002; Abdul-Karim *et al*., 2003).

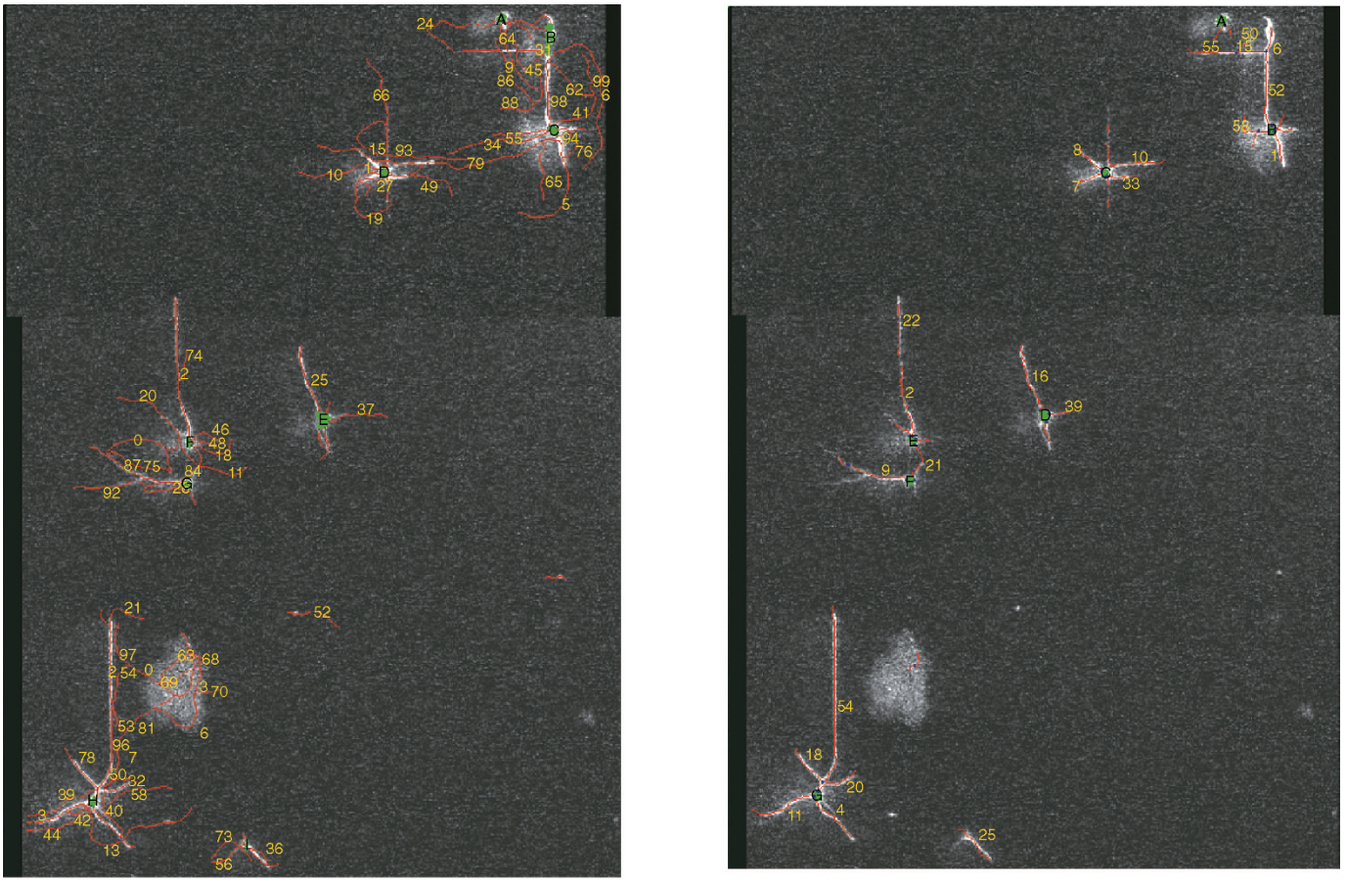

FIGURE 15.13. Illustrates the results of using mean template response (A), and the median template response (B) on noisy confocal images. Note the reduction in terms of erroneous false-positive traces when using the median template response. (image courtesy: IEEE Press.)

EXAMPLE COMBINING TUBE AND BLOB SEGMENTATION

One sometimes encounters images containing both blob-like and tube-like objects. From an image analysis standpoint, it is best to use distinctive fluorophores to highlight these two types of structures (e.g., Fig.15.5), and apply the appropriate analysis method to each image channel (Lin *et al.*, 2005). An example is shown in Figure 15.14(A), which shows an original image containing both blob-like objects (nuclei) in red and the tube-like cerebral vasculature in green. Figure 15.14(B) shows the resulting composite image after the separate segmentation of cell nuclei in the red channel and tracing of vasculature in the green channel. Figure 15.14(C) shows the original image containing blob-like objects (nuclei) in red and the cloud-like cytoskeleton in green. Figure 15.14(D) shows the resulting composite image after the segmentation of cell nuclei and cytoskeleton in the cytoplasm. After the initial image segmentation, a variety of postanalyses can be performed, such as morphometrics quantification, spatial analysis of different objects, object classification, and statistical analysis. Overall, these automated methods provide the useful tools for biologists replacing manual procedures that are tedious, subjective, and time consuming.

REGISTRATION AND MONTAGE SYNTHESIS METHODS

Registration is the process of spatially aligning two or more different images of the same region. When the object of interest is larger than the field-of-view of the microscope, two or more partially overlapping images must be acquired and then registered to provide an extended view of the specimen. Conversely, a sequence of images, taken at two different times, say before and after treatment, must then be registered to yield a common image subset to detect corresponding changes. Broadly, there are two approaches: landmark-based registration (Can *et al.*, 2002; Al-Kofahi *et al.*, 2003) and intensity-correlation based registration (Capek and Krekule, 1999; Beck *et al.*, 2000). Landmark-based registration relies on matching a set of distinctive points (landmarks) in pairs of the images in sequence, for example, spatially or temporally. Intensity-based registration methods work directly with the volumetric image data, utilizing all of the voxels. They compute a measure of correlation between the image pairs to estimate their relative spatial disposition. Finally, hybrid methods that combine ideas from landmark and intensity correlation methods are now emerging (Abu-Tarif, 2002). Most of these methods are well

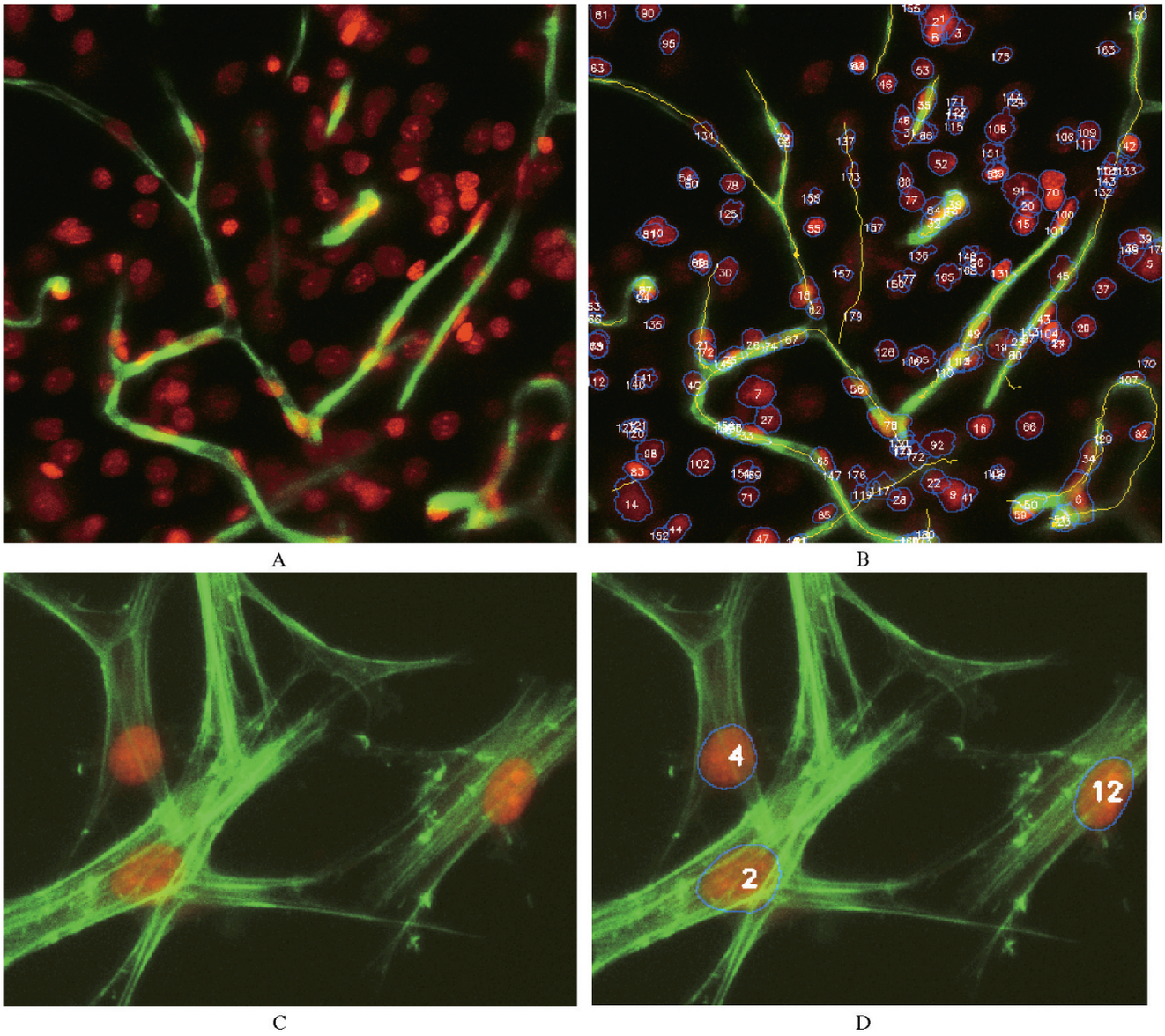

FIGURE 15.14. Image analysis examples illustrating (A) blob-like objects (nuclei) in red channel and tube-like objects (cerebral vasculature) in green channel; (C) blob-like objects (nuclei) in red channel and cloud-like objects (cytoskeleton) in the green channel. In both cases, image analysis is performed one spectral channel at a time, using separate methods for segmenting the blobs and tubes/clouds. Once this is done, it is possible to quantify the spatial relationships between the two kinds of objects. (data courtesy: Chris Bjornsson and Karen Smith at the Wadsworth Center, and Jan Stegemann Laboratory at Rensselaer.)

implemented in toolkit form, for example, the Insight toolkit from the National Library of Medicine (2001).

The transformation model used should have adequate degrees of freedom to account for motion and possible distortion between the two images (Hartley and Zisserman, 2000). For example, if only rigid body motion is considered between the two images, a rigid body transformation (rotation and translation) is adequate. However, if the anisotropic nature of the voxels and confocal system artifacts such as curvature of field and geometric distortions are present, a higher order transformation should be used. The affine model was proposed as a good compromise between model complexity and flexibility.

Landmark-based methods are generally fast and can scale up easily with higher-order transformation models, but their use is limited to the images where good landmarks can be extracted first. Centerline locations and branching points of tube-like objects (Al-Kofahi *et al*., 2003) and the centroids of blob-like objects (Becker *et al*., 1996) are examples of landmarks that can be used for registration. Although intensity-correlation–based methods do not require the landmark extraction step prior to registration, they are susceptible to imaging artifacts, such as non-uniform illumination, and do not exploit specific knowledge of the application context to simplify the problem. Furthermore, correlation-based algorithms are naturally far more computationally intensive than the landmark-based methods.

Montage synthesis, also known as mosaicing, is the process of stitching together a large number of partial local views ("windows") of the biological scene of interest to generate a more complete or extended field of view. This is especially valuable when the object/scene of interest is significantly larger than the

field of the microscope. The simplest type of montage synthesis consists of directly stitching together confocal images. Commonly, the microscope stage can be stepped in a series of overlapping two-dimensional (2D) or 3D windows that can then be merged into a single composite image that can be analyzed all at once. Alternatively, each of the windows can be subjected to automated image analysis, and the results stitched together to generate a synthetic montage-like representation. In addition to the common grayscale montage, it is possible to generate artificial representations such as segmentation label montages, and ball/stick diagrams, also known as object montages (Becker *et al*., 1996).

Another application for registration/montage synthesis is multi-view deconvolution (Cogswell *et al*., 1996; Heintzmann *et al*., 2000) and multi-view attenuation correction (Can *et al*., 2003). In the former, confocal images are blurred by the point spread function (PSF), which is asymmetric in the *x*-, *y*-, and *z*-dimensions. Multiple views can sometimes be used to account for the missing information and improve the axial resolution; ideally, we need tilted views separated by 90° angle. In the latter, the excitation/fluorescent light attenuates as a function of depth according to Beer's law (Weast, 1974) although spherical aberration is a more common cause of signal loss with depth. To correct for the attenuation, two views separated by 180° are used. In this scenario, the portions of one image with low signal-to-noise ratio (S/N) (far from the objective) are closer to the objective in the other image, with higher S/N, and vice versa (see also Chapter 37, *this volume*). These two images can be montaged to produce a more faithful representation of the entire specimen.

Figures 15.15 and 15.16 illustrate many of the issues described above. The neuron shown in Figure 15.15 was larger than the microscope field-of-view at the recording resolution. Also, the specimen was thick (more than 300 μm) which resulted in a significant signal loss for the deeper parts of the specimen. Montage synthesis was used to overcome these limitations; the specimen was mounted between two coverslips (Can *et al*., 2003) to allow imaging from both sides. The first image stack was captured in the conventional way, then the specimen was moved using the *x,y*-stage, and the second image stack was taken to capture the adjacent *x,y*-field. To correct for attenuation and to increase the imaging depth, the specimen was then flipped top-to-bottom, and two more sets of images were captured as before. Figure 15.16 shows the result of montaging the four image stacks with attenuation correction; the result is clearly a more faithful representation of the specimen. It captures the whole neuron, with high resolution and better S/N.

Finally, the microscopist is often faced with multi-channel data. Techniques for registering and montaging such data are

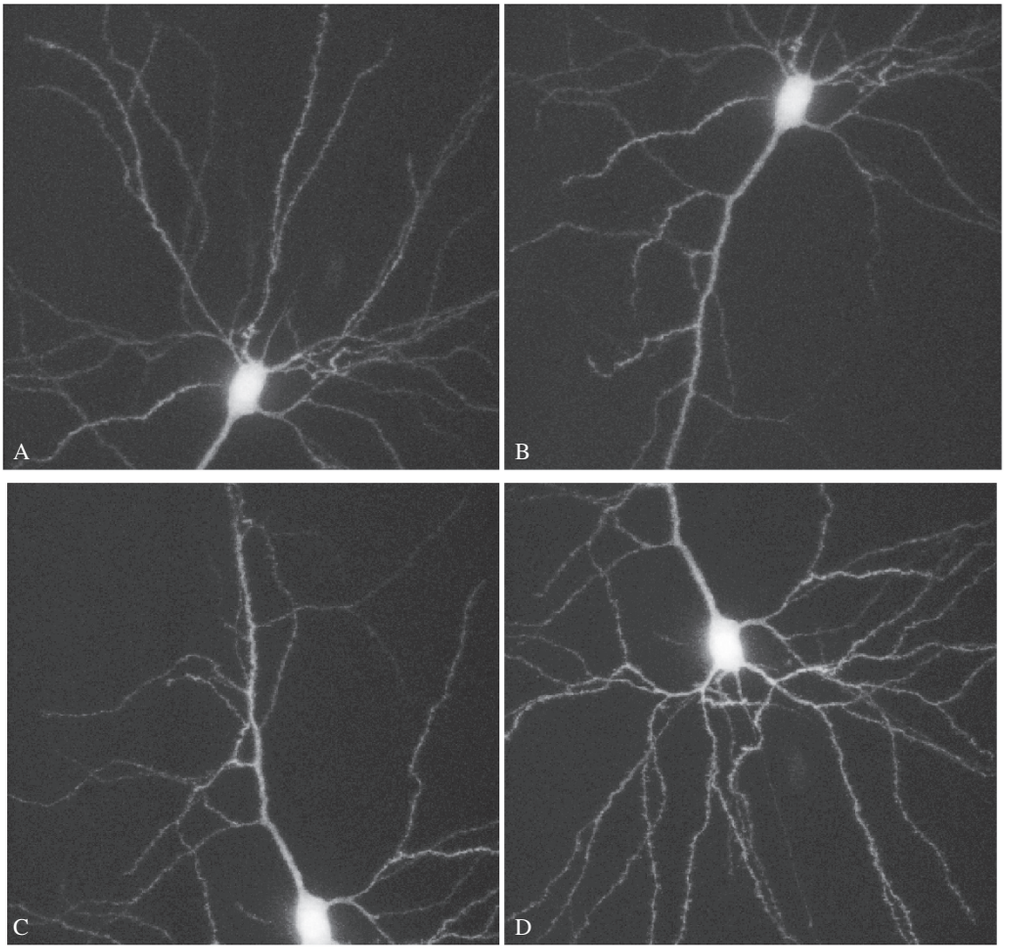

FIGURE 15.15. Sample views of an Alexa stained neuron from a rat brain. *X-y* maximum intensity projection. Top row, before flipping; the specimen was translated to capture the whole neuron between the positions in (A) and (B) respectively. Bottom row, after flipping; again, the specimen was translated to capture the whole neuron between the positions in (C) and (D) respectively. Each image is 512 × 480 × 261 voxels in size, except for the one in (C), 512 × 480 × 323 voxels. The neuron is larger than the microscope field of view, the four views cover the whole neuron maintaining high resolution. The sampling rates are 0.375 mm/voxel for x and y dimensions and 0.5 mm/voxel for the z dimension. (courtesy: Journal of Microscopy.)

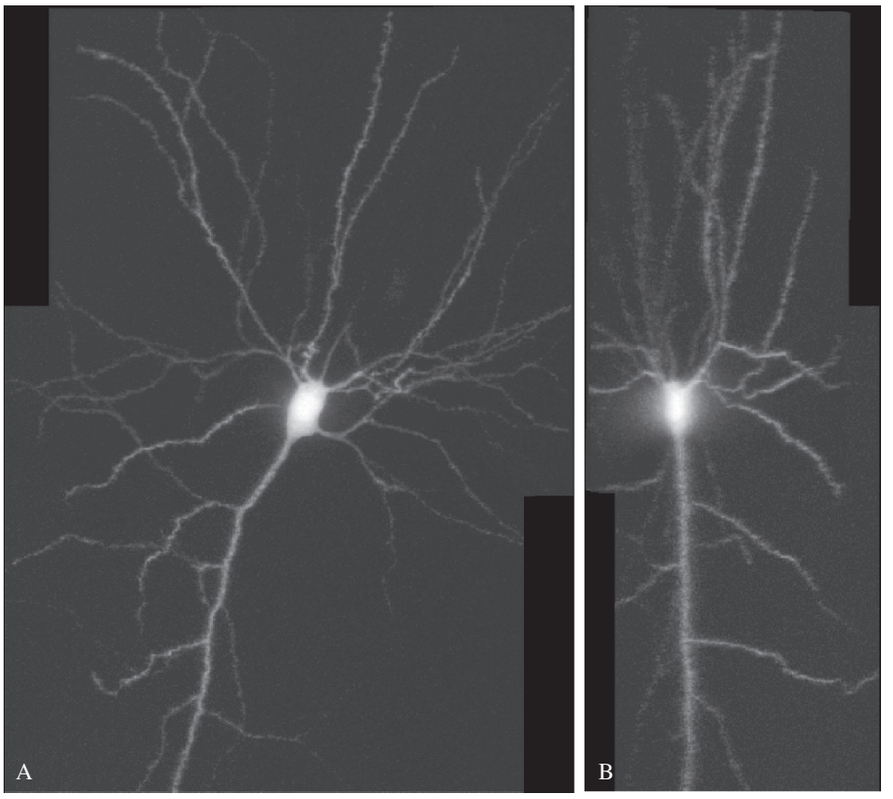

FIGURE 15.16. Mosaic image constructed from the four views in Figure 15.15 (A) top view (*x*-*y*), and (B) side view (*x*-*z*), maximum intensity projection. The result of the montaging is a high-resolution image for the whole neuron with increased effective imaging depth. (courtesy: Journal of Microscopy.)

analogous as long as corrections for chromatic aberration are performed. Figure 15.17(A) illustrates a two-channel mosaic representing one hemisphere of a rat brain section. The green regions are the nuclei and red color indicates the FISH signal. The full mosaic consists of 7911 × 6188 voxels (140 MB), and is synthesized from 70 imaging windows each of width 1024 × 1024 pixels. The inset is an enlarged view of a small portion of the montage at higher resolution. Figure 15.17(B) illustrates the montaging based on the traced vasculature structure.

METHODS FOR QUANTITATIVE MORPHOMETRY

Morphometric data are either the end goal of image analysis or an intermediate step towards testing a hypothesis. Listed below are common types of object measurements for blob-like and/or tube-like objects. Interested readers are referred to other books (Theodoridis and Koutroumbas, 1999; Shapiro and Stockman, 2001) for details on the algorithms needed to calculate these measurements.

- **Size measures**: Diameter, volume, surface area, length, width.
- **Intensity and spectral measurements**: Integrated, mean, and median intensity of one or more spectral channels over an object.
- **Shape measures**: Eccentricity, elongatedness, compactness, convexity, thickness, shape complexity, tortuosity, area-perimeter ratio, bending energy.
- **Texture measures**: Intensity variance, clumping, homogeneity.
- **Location and pose**: Centroid, major and minor axes, angle of tilt.
- **Interest points**: Convex/concave corners, inflexion points, bifurcations.
- **Invariants**: Dimensionless ratios such as shape factors, affine invariant moments.
- **Topological measures**: Branching factors and angles.
- **Group properties**: Group size and shape, repetition length.

Morphometric data can be generated from the segmented objects during segmentation or by postprocessing the segmentation results (Koh *et al*., 2002; Williams *et al*., 2003). In some cases, the segmentation algorithms that produce just a segmented volume may need postprocessing steps such as skeletonization (Lee *et al*., 1994; Maddah *et al*., 2003) to obtain the measurements. In the analysis of cellular compartment temporal activity by fluorescence *in situ* hybridization (catFISH) example, a set of measurements are made for each segmented nucleus. The measurements include nuclear features such as volume, intensity, texture, shape, and FISH measurements such as FISH spot volume, *z*-depth and intensity value, intranuclear and cytoplasmic FISH measurement, etc. Figure 15.1(B) shows a part of a spreadsheet containing such data. This data is ready for the statistical analysis required for hypothesis testing. It can also be used for manual evaluation to verify the accuracy of the automated results.

In the vessel tracing example, a region of interest is defined for each image of a time series data set by the intersection of the image and all other images in the set. Morphometric data collected within these regions include total vasculature length, average vasculature segment length, average horizontal width, and average vertical width, all extracted by the tracing algorithm. Statistics and traces generated outside these regions are ignored. The generated statistics are entered into a spreadsheet and plotted to highlight the changes. Actual change measurements such as percentage reduction in the total number of vasculature segments or percentage increase in the total vasculature length can be obtained directly from the spreadsheet.

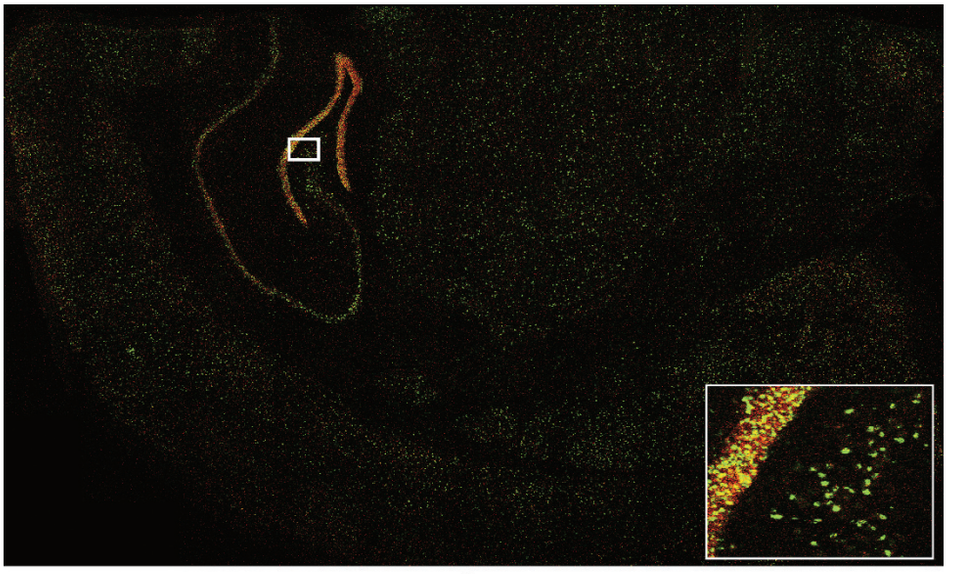

A

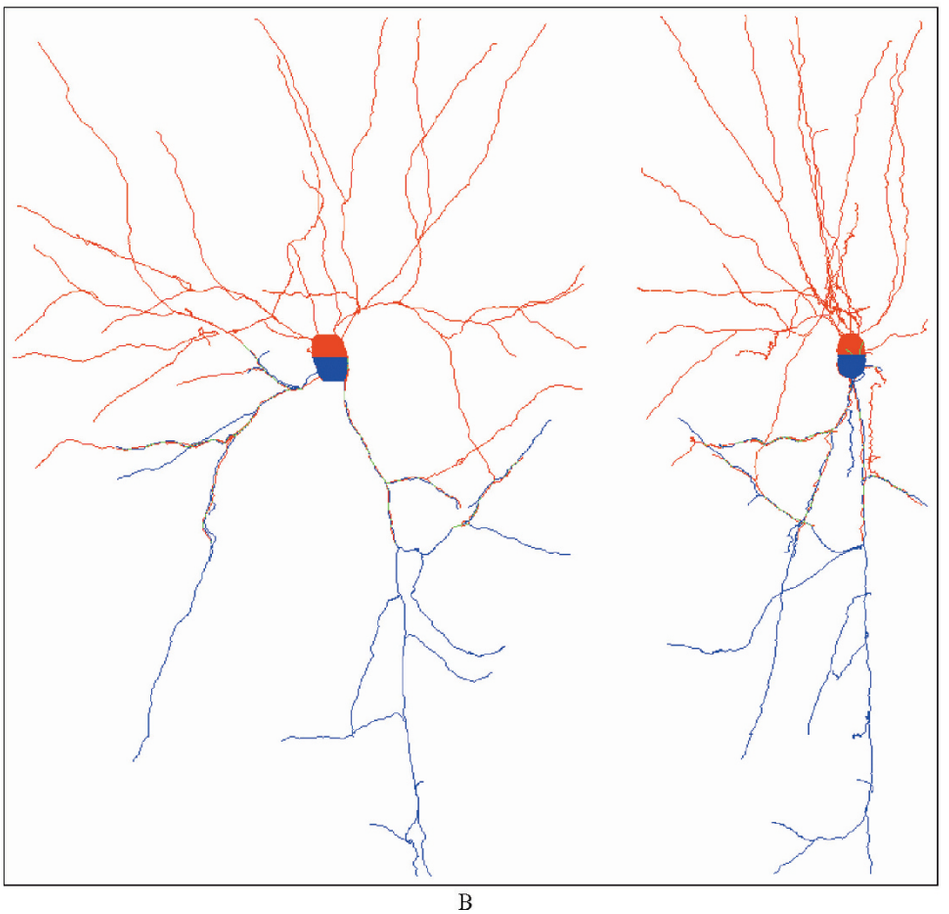

B

FIGURE 15.17. Illustrating the feature-based montaging of multi-spectral confocal microscope images. (A) Each individual image is first segmented, and a set of features (cell nuclei) are extracted from the segmented objects. These images are the basis of pairwise registration to montage the images. (B) Neurites are traced first, which become the basis of the montaging.

METHODS FOR VALIDATING THE SEGMENTATION AND MAKING CORRECTIONS

Validation can and should be performed at various stages of automatic image analysis. The main objective is to quantify the disagreement between automated results and the "ground truth," where a measurement of the disagreements is interpreted as the error. The ground truth is usually obtained manually. Being subjective, it is prone to inter- and intraobserver variability. This can be reduced by using multiple and independent manual segmentation results that are combined to approximate the ground truth. An effective method for combining the manual segmentations is to establish a consensus. For this, each disagreement between manual observers is resolved by careful discussion. Furthermore, the type of disagreement between the manual and automated results depends upon the type of objects.

For blobs, the types of errors include false detection (false positives), misses (false negatives), errors in separating connected objects, and errors in correctly delineating the boundaries of objects (Chawla *et al*., 2004). For tube-like objects, image analysis errors include falsely traced segments and branch points (false positives) and missed segments and branch points (false negatives), accuracy of the trace, accuracy of width measurements, and accuracy in locating branching/crossover points (Abu-Tarif *et al*., 2002; Al-Kofahi *et al*., 2003). When considering time-lapse series of live specimens (Abdul-Karim *et al*., 2003), it is also useful to quantify registration errors, and errors in detecting change.

As an example, the catFISH automated image analysis software was validated with respect to three criteria: (1) accuracy of nuclear segmentation, (2) accuracy in classifying intranuclear foci; and (3) accuracy in classifying cytoplasmic FISH signal. The manual image analysis was performed using MetaMorph software (Universal Imaging Corporation, West Chester, PA). Three separate experts manually rated each of the test image stacks for numbers of nuclei, nuclei that contained FISH signal, and cells that contained cytoplasmic FISH signal. Statistical analysis was done using a "consensus count" established by three experts.

Quantitative validation may also involve voxel-to-voxel comparisons of the segmented volume, or comparisons of any other entities derived from the segmented volume such as the vasculature centerline or the cell centroid. The comparison can be performed automatically to further reduce the subjectivity of validating the segmentation results (Al-Kofahi *et al*., 2002). In the case of tube-like objects, the centerline locations are extremely important because almost all morphometrics depend on them. Centerline locations are typically validated for the deviation from a "true" centerline (reflects the accuracy of the automated method), and the centerline coverage of the objects in the image (reflects how much manual editing the automated result needs). To obtain the accuracy metric, a distance map (Borgefors, 1986) can be used to calculate the average Euclidean distance between every voxel of manually segmented centerlines and every voxel of automatically segmented centerlines that are within a certain Euclidean distance.

Going further, validation of the extracted measurements from a segmented volume requires manual extraction of the measurements from the manually segmented volume. This is a prohibitively time-consuming procedure in 3D image analysis, and as the results will be subjective, it may not be useful. Instead, phantoms or artificial images are generated using ideal models (blobs, tubes, or clouds) of the biological objects with known morphometrics. Measurements are extracted automatically using the automated methods, and validated with the known values. Noise and other irregularities may be introduced to the phantoms to simulate actual images.

Manual editing is usually assisted by some software tools. Figure 15.2 shows the catFISH example of such software developed by this group. After manual validation obtained by consensus of several independent observers, automated segmentation results are further corrected using the convenient tools, such as buttons for add/delete, split/merge, and shrink/dilate in the catFISH system, as shown in Figure 15.18. Figure 15.19 illustrates the common editing to the tube-like object segmentation. Note that, by editing the automated results, the subjectivity factor of manual analysis is reduced down to the correspondence between manual and automated results.

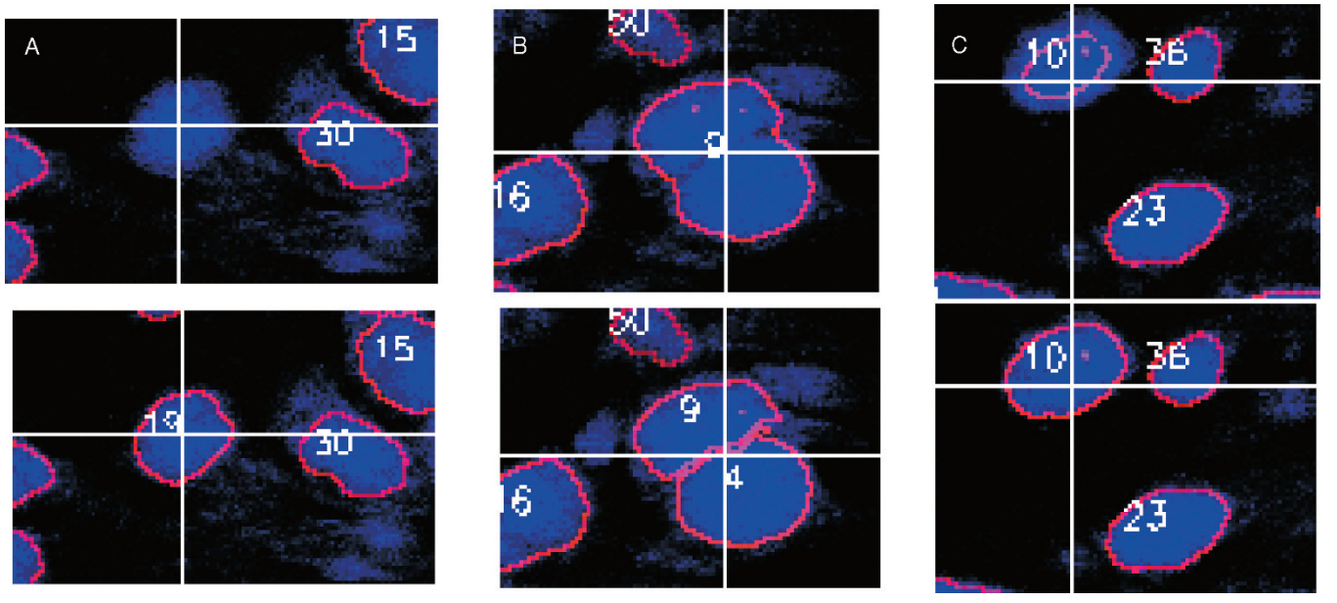

FIGURE 15.18. Illustrating common image analysis errors associated with blob segmentation, and manual editing tools to correct them: (A) Adding a missed object using a region growing tool; (B) Splitting connected objects; (C) Correcting a boundary location error.

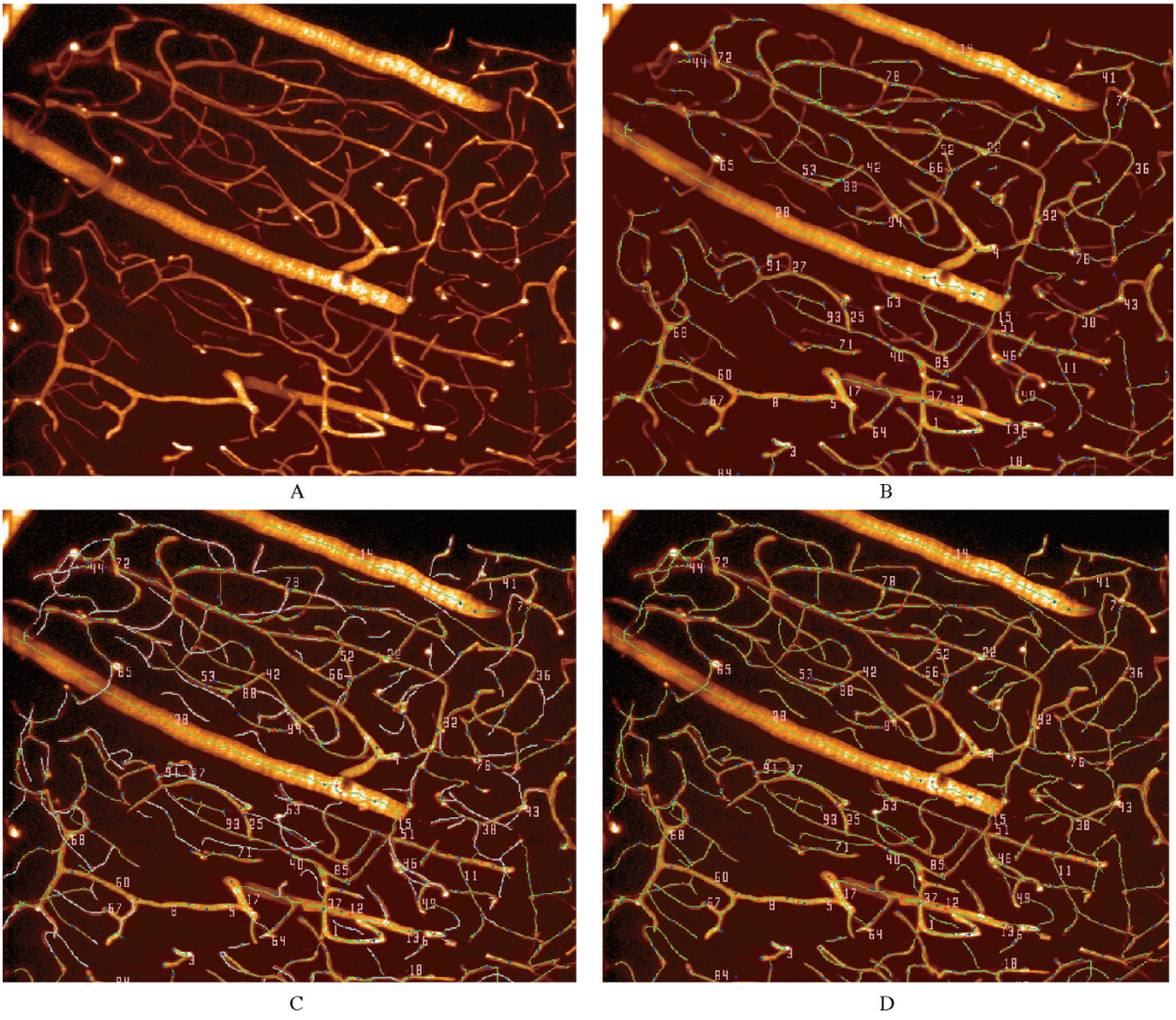

FIGURE 15.19. Illustrating the manual edits to the tube-like object segmentation. (A) Original image; (B) Automated tracing results; (C) Manually modified traces shown in light blue; (C) Final results.

ANALYSIS OF MORPHOMETRIC DATA

The statistical analysis of morphometric data is necessarily application-specific. The following paragraphs provide two examples illustrating the main ideas.

In the catFISH system, the important goal is to classify the nuclei in the image based on the presence of the intranuclear and cytoplasmic FISH signal. The measurements are integrated and associated spatially with the nuclear segmentation results to generate a detailed tabular/database representing the location and detailed morphometric parameters for each nucleus, and the associated FISH signals. Nucleus class information is defined by the user according to some criteria such as the color channels, presence or absence of signal, and location of the signal. The software uses this information to automatically classify each nucleus as negative or as containing intranuclear and/or cytoplasmic FISH signal based upon its morphometric and functional (FISH) measurements. The final result is output into a text file including total nuclear count and the number and percentage of nuclei in each class.

In the angiogenesis example, the primary intent is to quantitate temporal vessel changes in a set of time-series images. There are two broad methods for change analysis. One method is to compute morphometric data from images at each temporal sampling point, and to perform a statistical comparison of these data. A more ambitious approach is to register the images over time and extract detailed changes on a vessel-segment by vessel-segment basis. In this work, the less ambitious approach was adopted as a starting point. Vessel lengths, widths, and count can be readily obtained from the traces generated by the automatic tracing algorithm described. Naturally, only vasculature segments located in the volume common to all four images contributed to these statistics. An overall Change Index is calculated as the simple ratio of the current measurement over the previous measurement.

DISCUSSION, CONCLUSION, AND FUTURE DIRECTIONS

We have attempted to summarize techniques for automated 3D image analysis by organizing the methods into those suitable for a small number of categories of features (blobs, tubes, clouds, mixed). By recognizing image objects along these lines, the reader is better able to select from the available image analysis tools. It has also served as the basis for organizing image analysis packages such as the catFISH system.

The life-sciences researcher is often able to perform automated 2D image analysis using off-the-shelf software, for example, NIH Image, MetaMorph by Universal Imaging, and VoxelView by Vital Images (more examples discussed in Chapter 14, *this volume*). The sheer complexity and variability of biological imagery and the current state of evolution of automated 3D image analysis technology imply that the assistance of an image analysis specialist is often called for. It is hoped that the terminology and language presented here can bridge these disciplines. The organization of image analysis by type of objects also forms a good basis for facilitating productive discussion between life-sciences researchers and computer scientists.

Automated image analysis is a dynamic computer-intensive discipline. It has benefited tremendously from problems posed by life-science researchers. Much work remains to be done. For example, the algorithms are still not nearly as adaptive as the human visual system. Given a novel set of image data, the human observer can be trained much more quickly than new image analysis tools can be designed and tested. Nevertheless, development of new tools is worthwhile whenever large amounts of data must be processed, for instance, in the development of high-content screening assay as described in Chapter 46, *this volume*. This chapter has accordingly devoted attention to studies that require this type of sophisticated automation.

ACKNOWLEDGMENTS

The work described here was funded by a number of sponsors. Recent sponsorships include the National Science Foundation (award EEC-9986821 and various supplements), the National Institutes of Health (awards AG18230), MARA of Malaysia, and by MicroBrightfield Inc. This work was also partially supported by the Nanobiotechnology Center (NBTC), an STC Program of the National Science Foundation under Agreement No. ECS-9876771, and by grant NINDS 8R01EB-000359 from the National Institutes of Health.

The authors are grateful to a number of colleagues who have contributed data and insight leading to this book chapter. The catFISH example is drawn from collaborative work with Carol Barnes, John Guzowski, Kathy Olson, Monica Chawla, and Almira Vazarjanova at the University of Arizona, and Umesh Adiga at the Lawrence Berkeley Laboratory. The angiogenesis example is drawn from collaborative efforts with Rakesh K. Jain and Edward Brown at Massachusetts General Hospital. The neuron tracing examples are drawn from collaborations with Christopher Pace, Natalie Dowell, Chris Bjornsson, Danielle LeBlanc, and Karen Smith at the Wadsworth Center, and George Nagy at Rensselaer. The image registration examples are drawn from collaborative work with Ali Can and Hanu Singh at the Woods Hole Oceanographic Institute, and Charles Stewart at Rensselaer. The example in Figure 15.14 is drawn from collaborative projects with Jan Stegemann and Sung-Yun Lee at Rensselaer Polytechnic Institute.

REFERENCES

Abdul-Karim, M.-A., Al-Kofahi, K., Brown, E.B., Jain, R.K., and Roysam, B., 2003, Automated tracing and change analysis of angiogenic vasculature from in vivo multiphoton confocal image time series, *Microvasc. Res.* 66:113–125.

Abdul-Karim, M.-A., Roysam, N.M., Dowell-Mesfin, A., Jeromin, M., Yuksel, M., and Kalyanaraman, S., 2005, Automatic selection of parameters for vessel/neurite segmentation algorithms. *Image Processing, IEEE Trans.* 14(9):1338–1350.

Abu-Tarif, and Ahmad A., 2002, Volumetric registration based on intensity and geometry features, PhD Thesis, Rensselaer Polytechnic Institute, Troy, New York.

Adams, R., and Bischof, L., 1994, Seeded region growing, *IEEE Trans. Pattern Anal. Machine Intell.* 16:641–647.

Adiga, U., and Chaudhuri, B., 2001a, An efficient method based on watershed and rule-based merging for segmentation of 3D histo-pathological images, *Pattern Recognition* 34:1449–1458.

Adiga, U., and Chaudhuri, B., 2001b, Some efficient methods to correct confocal images for easy interpretation, *Micron* 32:363–370.

Al-Kofahi, K.A., Lasek, S., Szarowski, D.H., Pace, J., Nagy, G., Turner, J.N., and Roysam, B., 2002, Rapid automated three-dimensional tracing of neurons from confocal image stacks, *IEEE Trans. Inform. Technol. Biomed.* 6:171–187.

Al-Kofahi, O., Can, A., Lasek, S., Szarowski, D.H., Turner, J.N., and Roysam, B., 2003, Algorithms for accurate 3D registration of neuronal images acquired by confocal scanning laser microscopy, *J. Microsc.* 211:8–18.

Ancin, H., Roysam, B., Dufresne, T.E., Chestnut, M.M., Ridder, G.M., Szarowski, D.H., and Turner, J.N., 1996, Advances in automated 3-D image analyses of cell populations imaged by confocal microscopy, *Cytometry* 25:221–234.

Ballard, D.H., and Brown, C.M., 1982, *Computer Vision*, Prentice Hall, Englewood Cliffs, New Jersey.

Beck, J.C., Murray, J.A., Willows, A.O., and Cooper, M.S., 2000, Computer-assisted visualizations of neural networks: Expanding the field of view using seamless confocal montaging, *J. Neurosci. Methods* 98:155–163.

Becker, D.E., Ancin, H., Szarowski, D.H., Turner, J.N., and Roysam, B., 1996, Automated 3-D montage synthesis from laser-scanning confocal images: application to quantitative tissue-level cytological analysis, *Cytometry* 25:235–245.

Besl, P.J., and Jain, R.C., 1988, Segmentation through variable-order surface fitting, *IEEE Trans. Pattern Anal. Machine Intell.* 10:167–192.

Beucher, S., 1982, Watersheds of functions and picture segmentation, *IEEE International Conference on Acoustics, Speech, and Signal Processing*, pp. 1928–1931.

Beucher, S., 1991, The watershed transformation applied to image segmentation, *Conference on Signal and Image Processing in Microscopy and Microanalysis*, Cambridge, UK, pp. 299–314.

Bhanu, B., 1982, Shape matching and image segmentation using stochastic labeling, Los Angeles Image Processing Institute.

Bhanu, B., and Lee, S., 1994, *Genetic Learning for Adaptive Image Segmentation*, Kluwer Academic Publishers, Boston.

Bhattacharjya, A., and Roysam, B., 1994, Joint solution of low, intermediate and high-level vision tasks by evolutionary optimization: Application to computer vision at low SNR, *IEEE Trans. Neural Networks* 5:83–95.

Black, M., and Rangarajan, A., 1996, On the unification of line processes, outlier rejection, and robust statistics with applications in early vision, *Int. J. Comput. Vis.* 19(1).

Blake, A., and Zisserman, A., 1987, *Visual Reconstruction*, MIT Press, Cambridge, Massachusetts.

Borgefors, G., 1986, Distance transformations in digital images, *Comput. Vis. Graphics Im. Pract.* 34:344–371.

Bovik, A.C., Aggarwal, S.J., Merchant, F., Kim, N.H., and Diller, K.R., 2001, Automatic area and volume measurements from digital biomedical images. In: *Image Analysis: Methods and Applications* (D.-P. Häder, ed.), CRC Press, Boca Raton, Florida, pp. 23–64.

Brown, E.B., Campbell, R.B., Tsuzuki, Y., Xu, L., Carmeliet, P., Fukumura, D., and Jain, R.K., 2001, In vivo measurement of gene expression, angiogenesis and physiological function in tumors using multi-photon laser scanning microscopy, *Nat. Med.* 7:864–868.

Can, A., Al-Kofahi, O., Lasek, S., Szarowski, D.H., Turner, J.N., and Roysam, B., 2003, Attenuation correction in confocal laser microscopes: A novel two-view approach, *J. Microsc*. 211:67–79.

Can, A., Shen, H., Turner, J.N., Tanenbaum, H.L., and Raysam, B., 1999, Rapid automated tracing and feature extraction from retinal fundus images using direct exploratory algorithms, *IEEE Trans. Inform. Technol. Biomed*. 3:125–138.

Can, A., Stewart, C.V., Roysam, B., and Tanenbaum, H.L., 2002, A feature-based, robust, hierarchical algorithm for registering pairs of images of the curved human retina, *IEEE Trans. Pattern Anal. Machine Intell*. 24:347–364.

Capek, M., and Krekule, I., 1999, Alignment of adjacent picture frames captured by a CLSM, *IEEE Trans. Inform. Technol. Biomed.* 3:119–124.

Capowski, J.J., 1989, *Computer Techniques in Neuroanatomy*, Plenum Press, New York.

Castleman, K., 1996, *Digital Image Processing*, Prentice-Hall, Englewood Cliffs, New Jersey.

Chang, Y.-L., and Li, X., 1994, Adaptive image region-growing, *IEEE Trans. Image Processing* 3:868–872.

Chawla, M.K., Lin, G., Olson, K., Vazdarjanova, A., Burke, S.N., McNaughton, B.L., Worley, P.F., Guzowski, J.F., Roysam, B., and Barnes, C.A., 2004, 3D-catFISH: A system for automated quantitative three-dimensional compartmental analysis of temporal gene transcription activity imaged by fluorescence in situ hybridization, *J. Neurosci. Methods* 139:13–24.

Cogswell, C.J., Larkin, K.G., and Klemn H.U., 1996, Fluorescence microtomography: Multiangle image acquisition and 3D digital reconstruction. In: *Three-Dimensional Microscopy: Image Acquisition and Processing III*, SPIE, San Jose, California.

Cohen, A.R., Roysam, B., and Turner, J.N., 1994, Automated tracing and volume measurements of neurons from 3-D confocal fluorescence microscopy data, *J. Microsc*. 173:103–114.

Cooper, M., 1998, The tractability of segmentation and scene analysis, *Image and Vision Computing* 30(1):27–42.

Cootes, T.F., Taylor, C., Cooper, D., and Graham, J., 1995, Active shape models — Their training and application, *Comput. Vis. Image Understanding* 61:38–59.

Davis, L., 1975, A survey of edge detection techniques, *Comput. Graphics Image Process*. 4(3):248–270.

di Zenzo, S., 1983, Advances in image segmentation, *Image and Vision Computing* 1:196–210.

Digabel, H., and Lantuejoul, C., 1978, Iterative algorithms, *Pract. Methods* 8:85–99.

Dillencourt, M., Samet, H., and Tamminen, M., 1992, A general approach to connected-components labeling for arbitrary image representations, *J. ACM* 39:253–280.

Dougherty, E.R., 1993, Mathematical Morphology in Image Processing, Marcel Dekker, New York.

Fu, K., and Mui, J., 1981, A survey of image segmentation, *Pattern Recognition* 13:3–16.

Ghanei, A., and Soltanian-Zadeh, H., 2002, A discrete curvature-based deformable surface model with application to segmentation of volumetric images, *IEEE Trans. Inform. Technol. Biomed*. 6:285–295.

Glaser, J.R., and Glaser, E.M., 1990, Neuron imaging with Neurolucida — A PC-based system for image combining microscopy, *Comput. Med. Imaging Graphics* 14:307–317.

Gong, W., and Bertrand, G., 1990, A note on thinning of 3-D images using sage point thinning algorithm, *Pattern Recogn. Lett*. 11:499–500.

Guigues, L., Le Men, H., and Cocquerez, J.-P., 2003, The hierarchy of the cocoons of a graph and its application to image segmentation, *Pattern Recogn. Lett*. 24:1059–1066.

Guzowski, J., and Worley, P., 2001, *Cellular Compartment Analysis of Temporal Activity by Fluorescence In Situ Hybridization (catFISH)*, John Wiley and Sons, New York.

Guzowski, J.F., McNaughton, B.L., Barnes, C.A., and Worley, P.F., 1999, Environment-specific expression of the immediate-early gene Arc in hippocampal neuronal ensembles, *Nat. Neurosci*. 2:1120–1124.

Haddon, J.F., and Boyce, J.F., 1993, Co-occurrence matrices for image analysis, *Electron Commun. Eng.* J. 5:71–83.

Haralick, R., and Shapiro, L., 1985, Image segmentation techniques, *Computer Vision Graphics and Image Processing* 29:100–132.

Hartley, R., and Zisserman, A., 2000, Multiple View Geometry in Computer Vision, Cambridge University Press, New York.

He, W., Hamilton, T.A., Cohen, A.R., Holmes, T.J., Pace, C., Szarowski, D.H., Turner, J.N., and Roysam, B., 2003, Automated three-dimensional tracing of neurons in confocal and brightfield images, *Microsc. Microanal*. 9:296–310.

Heintzmann, R., Kreth, G., Cremer, C., 2000, Reconstruction of axial tomographic high resolution data from confocal fluorescence microscopy: A method for improving 3D FISH images, *Anal. Cell. Pathol*. 20:7–15.

Higgins, W., and Ojard, E., 1993, Interactive morphological watershed analysis for 3D medial images, *Comput. Med. Imaging Graphics* 17:387–395.

Hojjatoleslami, S.A., and Kittler, J., 1998, Region growing: A new approach, *IEEE Trans. Image Processing* 7:1079–1084.

Horowitz, S., and Pavlidis, T., 1974, Picture segmentation by a directed split and merge procedure. International Conference on Pattern Recognition, Copenhagen, Denmark, pp. 424–433.

Howard, V., and Reed, M.G., 1998, *Unbiased Stereology: Three-Dimensional Measurement in Microscopy*, Springer-Verlag, New York.

Howard, V., Reid, S., Baddeley, A., and Boyde, A., 1985, Unbiased estimation of particle density in the tandem scanning reflected light microscope, *J. Microsc*. 138:203–212.

Huber, P.J., 1981, *Robust Statistics*, John Wiley and Sons, New York.

ITK, 2001, *NLM Insight Segmentation and Registration Toolkit*, available at: http://www.itk.org.

Jaeger, D., 2000, Accurate reconstruction of neuronal morphology, In: *Computational Neuroscience: Realistic Modeling for Experimentalists* (E.D. Schutter, ed.), CRC Press, Boca Raton, Florida, pp. 159–178.

Jain, R.K., Munn, L.L., and Fukumura, D., 2002, Dissecting tumour pathophysiology using intravital microscopy, *Nat. Rev. Cancer* 2:266–276.

Kanade, T., 1978, Region segmentation: signal vs. semantics, International Conference on Pattern Recognition.

Kerfoot, I., and Bresler, Y., 1999, Theoretical analysis of multispectral image segmentation criteria, *IEEE Trans. Image Process*. 8(6):798.

Kim, B., Kim, D., and Park, D., 2001, Novel precision target detection with adaptive thresholding for dynamic image segmentation, *Machine Vis. Appl*. 12:259–270.

Koh, I.Y., Lindquist, W.B., Zito, K., Nimchinsky, E.A., and Svoboda, K., 2002, An image analysis algorithm for dendritic spines, *Neural Comput*. 14:128–1310.

Lee, T.C., Kashyap, R.L., and Chu C.N., 1994, Building skeleton models via 3-D medial surface axis thinning algorithms, *Graphic. Models Image Process*. 56:462–478.

Lin, G., Adiga, U., Olson, K., Guzowski, J., Barnes, C., and Roysam, B., 2003, A hybrid 3-D watershed algorithm incorporating gradient cues and object models for automatic segmentation of nuclei in confocal image stacks, *Cytometry* 56A:23–36.

Lin, G., Bjornsson C.S., Smith, K.L., Abdul-Karim, M.A., Turner, J.N., Shain, W., and Roysam, B., 2005, Automated image analysis methods for 3D quantification of the neurovascular unit from multi-channel confocal microscope images. *Cytometry* 66(1):9–23.

Lin, G., Chawla, M.K., Olson, K., Guzowski, J.F., Barnes, C.A., and Roysam, B., 2004, Hierarchial, model-based merging of multiple fragments for 3-D segmentation of nuclei, *Cytometry* DOI: 10.1002/cyto.a.20099.

Lorigo, L.M., Faugeras, O.D., Grimson, W.E., Keriven, R., Kikinis, A., Nabavi, A., and Westin, C.F., 2001, CURVES: Curve evolution for vessel segmentation, *Med. Image Anal*. 5:195–206.

Mackin, R., Roysam, B., Holmes, T., and Turner, J., 1993, Automated image analysis of thick cytological preparations using 3-D microscopy and 3-D image analysis: Applications of pap smears, *Anal. Quant. Cytol. Histol*. 15:405–417.

Maddah, M., Afzali-Kusha, A., and Soltanian-Zedeh, H., 2003, Efficient centerline extraction for quantification of vessels in confocal microscopy images, *Med. Phys.* 30:204–211.

Maisonneuve, F., 1982, Sue le partage des eaux, Technical report School of Mines.

Malpica, N., de Solorzano, C.O., Vaquero, J.J., Santos, A., Vallcorba, I., Garcia-Sagredo, J.M., and del Pozo, F., 1997, Applying watershed algorithms to the segmentation of clustered nuclei, *Cytometry* 28:289–297.

Marko, M., and Leith, A., 1992, Contour based 3-D surface reconstruction using stereoscopic contouring and digitized images, In: *Visualization in Biomedical Microscopics: 3-D Imaging and Computer Applications* (A. Kriete, ed.), VCH, Weinheim, Germany, pp. 45–74.

McInerney, T., and Terzopoulos, D., 1996, Deformable models in medical image analysis: A survey, *Med. Image Anal*. 1:91–108.

Mitiche, A., and Aggarwal, J., 1985, Image segmentation by conventional and information-integrating techniques: A synopsis, International Conference on Pattern Recognition 3:50–62.

Morel, J.-M., and Solimini, S., 1995, Variational Methods in Image Segmentation: With Seven Image Processing Experiments, Birkhèauser, Boston.

Mouton, P.R., 2002, *Principles and Practices of Unbiased Stereology: An Introduction for Bioscientists*, Johns Hopkins University Press, Baltimore.

Neumann, A., 2003, Graphical Gaussian shape models and their application to image segmentation, *IEEE Trans. Pattern Anal. Machine Intell*. 25:316–329.

Nevatia, R., 1986, Image segmentation, *Handbook of Pattern Recognition and Image Processing* 86.

Pavlidis, T., 1977, *Structural Pattern Recognition*, Springer-Verlag, Berlin, Germany.

Pavlidis, T., and Liow, Y.-T., 1990, Integrating region growing and edge detection, *IEEE Trans. Pattern Anal. Machine Intell*. 12:225–233.

Pawley, J., 2000, The 39 steps: A cautionary tale of quantitative 3-D fluorescence microscopy, *Bioimaging Biotechn*. 28:884–888.

Pham, D.L., Xu, C., and Prince, J.L., 2000, Current methods in medical image segmentation, Annu. Rev. Biomed. Eng. 2:315–337.

Ranade, S., and Prewitt, J., 1980, A comparison of some segmentation algorithms for cytology, *ICPR* 80.

Raya, S.P., and Udupa, J.K., 1990, Shape-based interpolation of multidimensional objects, *IEEE Trans. Med. Imaging* 9:32–42.

Rezaee, M.R., 1998, Application of fuzzy techniques in image segmentation, PhD thesis, University of Leiden, Leiden, The Netherlands.

Rosenfeld, A., and Davis, L., 1979, Image segmentation and image models, Proc. IEEE 67:764–772.

Roysam, B., Ancin, H., Bhattacharjya, A., Chisti, M., Seegal, R., and Turner, J., 1994, Algorithms for automated cell population analysis in thick specimens from 3-D confocal fluorescence microscopy data, *J. Microsc*. 173:115–126.

Roysam, B., Bhattacharjya, A., Srinivas, C., and Turner, J., 1993, Unsupervised noise removal algorithms for 3-D confocal fluorescence microscopy, *Micron Microscopica Acta* 23:447–461.

Roysam, B., and Miller, M., 1992, Combining stochastic and syntactic processing with analog computation methods, *Digital Signal Process*. 2:48–64.

Russ, J.C., 1994, *The Image Processing Handbook*, CRC Press, Boca Raton, Florida.

Russ, J.C., and DeHoff, R.T., 2000, *Practical Stereology*, Kluwer Academic/Plenum, New York.

Sahoo, P., Soltani, S., Wong, A., and Chen, Y., 1988, A survey of thresholding techniques, *Comput. Vis. Graphics Image Process*. 41:233–260.

Sarti, A., Ortiz de Solorzano, C., Lockett, S., and Malladi, R., 2000, A geometric model for 3-D confocal image analysis, *IEEE Trans. Biomed. Eng*. 47:1600–1609.

Sato, Y., Nakajima, S., Shiraga, N., Atsumi, H., Yoshida, S., Koller, T., Gerig, G., and Kikinis, R., 1998, Three-dimensional multi-scale line filter for segmentation and visualization of curvilinear structures in medical images, *Med. Image Anal*. 2:143–168.

Serra, J.P., and Soille, P., 1994, *Mathematical Morphology and Its Applications to Image Processing*, Kluwer Academic Publishers, Boston.

Shafarenko, L., Petrou, M., and Kittler, J., 1997, Automatic watershed segmentation of randomly textured color images, *IEEE Trans. Image Processing* 6:1530–1544.

Shain, W., Turner, J., Szarowski, D., Davis-Cox, M., Ancin, H., and Roysam, B., 1999, Application and quantitative validation of computer-automated 3-D counting of cell nuclei in brain tissue, *Microsc. Microanal*. 5:106–119.

Shapiro, L.G., and Stockman, G.C., 2001, *Computer Vision*, Prentice Hall, Upper Saddle River, New Jersey.

Sijbers, J., Scheunders, P., Verhoye, M., van der, L.A., van Dyck, D., and Raman, E., 1997, Watershed-based segmentation of 3D MR data for volume quantization, *Magn. Reson. Imaging* 15:679–688.

Sklansky, J., 1978, Image segmentation and feature extraction, *IEEE Transactions on Systems, Man, and Cybernetics* 8:237–247.

So, P.T., Dong, C.Y., Masters, B.R., and Berland, K.M., 2000, Two-photon excitation fluorescence microscopy, *Annu. Rev. Biomed. Eng*. 2:399–429.

Solorzano, C., and Rodriguez, E., 1999, Segmentation of confocal microscope images of cell nuclei in thick tissue sections, *J. Microsc*. 193:212–226.

Staib, L.H., and Duncan, J.S., 1996, Model-based deformable surface finding for medical images, *IEEE Trans. Medical Imaging* 15:720–731.

Streekstra, G.J., and van Pelt, J., 2002, Analysis of tubular structures in three-dimensional confocal images, *Network* 13:381–395.

Sun, Y., Lucariello, R.J., and Chiaramida, S.A., 1995, Directional low-pass filtering for improved accuracy and reproducibility of stenosis quantification in coronary arteriograms, *IEEE Trans. Medical Imaging*, 14:242–248.

Sunil Kumar, K., and Desai, U., 1999, Joint segmentation and image interpretation, *Pattern Recognition* 32:577–589.

Suri, J.S., Setarehdan, S.K., and Singh, S., 2002, Advanced algorithmic approaches to medical image segmentation: state-of-the-art applications in cardiology, neurology, mammography, and pathology, Springer-Verlag, New York.

Theodoridis, S., and Koutroumbas, K., 1999, *Pattern Recognition*, Academic Press, New York.

Trucco, E., and Fisher, R.B., 1995, Experiments in curvature-based segmentation of range data, *IEEE Trans. Pattern Anal. Machine Intell*. 17:177–182.

Tsao, Y., and Fu, K., 1981, A parallel thinning algorithm for 3-D pictures, *Comput. Graphics Image Process.* 17:315–331.

Valeur, B., 2002, *Molecular Fluorescence: Principles and Applications*, Wiley-VCH, Weinheim, Germany.

Vazdarjanova, A., McNaughton, B.L., Barnes, C.A., Worley, P.F., and Guzowski, J.F., 2002, Experience-dependent coincident expression of the effector immediate-early genes arc and Homer 1a in hippocampal and neocortical neuronal networks, *J. Neurosci*. 22:10067–10071.

Vemuri, B., and Radisavljevic, A., 1994, Multiresolution stochastic hybrid shape models with fractal priors, *ACM Trans. Graphics* 13:177–207.

Vincent, L., 1993, Morphological grayscale reconstruction in image analysis: Applications and efficient algorithms, *IEEE Trans. Image Processing* 2:176–201.

Vincent, L., and Soille, P., 1991, Watersheds in digital spaces: An efficient algorithm based on immersion simulations, *IEEE Trans. on Pattern Analysis and Machine Intelligence*, 13(6):583–598.

Weast, R.C., 1974, *Handbook of Chemistry and Physics; A Ready-Reference Book of Chemical and Physical Data*, Chemical Rubber Company, Cleveland, Ohio.

Weichert, F., Müller, H., Quast, U., Kraushaar, A., Spilles, P., Heintz, M., Wilke, C., van Birgelen, C., Erbel, R., and Wegener, D., 2003, Virtual 3D IVUS vessel model for intravascular brachytherapy planning. I. 3D segmentation, reconstruction, and visualization of coronary artery architecture and orientation, *Med. Phys*. 30:2530–2536.

Williams, J., Tek, H., Comaniciu, D., and Avants, B., 2003, Three-dimensional interactive vascular postprocessing techniques: Industrial perspective. In: *Angiography and Plaque Imaging: Advanced Segmentation Techniques* (J.S. Suri and S. Laxminarayan, eds.), CRC Press, Boca Raton, Florida, pp. 99–142.

Wilson, R., and Spann, M., 1988, *Image Segmentation and Uncertainty*, John Wiley and Sons, New York.

Ying, X., and Uberbacher, E.C., 1997, 2D image segmentation using minimum spanning trees, *Image Vis. Comput*. 15:47–57.

Zhu, S.C., and Yuille, A., 1996, Region competition: Unifying snakes, region growing, and Bayes/MDL for multiband image segmentation, *IEEE Trans. Pattern Anal. Machine Intell*. 18:884–900.

Zucker, S., 1977, Algorithms for image segmentation, Digital Image Processing and Analysis, 77:169–183.

Zucker, S.W., 1976, Region growing: Childhood and adolescence, *Comput. Vis. Graphics Image Process*. 5:382–399.